Physics design of a saddle coil system for TCV

J. X. Rossel*, J.-M. Moret, Y. Martin, G. Pochon, the TCV team [1]

Ecole Polytechnique Fédérale de Lausanne (EPFL)
Centre de Recherches en Physique des Plasmas
Association Euratom-Confédération Suisse
CH-1015 Lausanne, Switzerland

Abstract

The upgrade project for **TCV** (Tokamak à Configuration Variable) includes the installation of a set of saddle coils, namely the saddle coil system (**SCS**), located and powered such as to create a helical magnetic perturbation. Using independent power supplies, the toroidal periodicity of this perturbation is tunable, allowing simultaneously edge localized modes (**ELM**) control through resonant magnetic perturbation (**RMP**), error field correction and vertical control. Other experimental applications, like resistive wall mode and rotation control, are also in view. In this article, the adequacy of two SCS designs, an in-vessel one and an ex-vessel one, is assessed with respect to the desired experimental applications. The current requirements and the system performances are also characterized. The conducting vessel wall is accounted for in a model used to determine the coupled response functions of the SCS, the screening of the magnetic perturbation by the wall, the induced voltages and currents during a plasma disruption and the maximal magnetic forces exerted on the SCS. A scaling of the SCS parameters with the number of coil turns is presented and the issue of coil heating and cooling is discussed.

Keywords: tokamak, saddle coil, edge localized mode, resonant magnetic perturbation, error field, vertical control

*Tel.: +41 21 693 22 63; Fax.: +41 21 693 51 76.
Email address: jonathan.rossel@epfl.ch (J. X. Rossel)

1. Introduction

Edge localized modes [2], related to the high confinement regime (H-mode) [3], lead to a degradation of the plasma confinement and a release of energetic particles toward the vessel walls. Scaling the current experimental data to ITER predicts that the power flux released by ELMs will cause an intolerable erosion and heat load on the plasma facing components [4, 5]. Experiments on DIII-D [6, 7], JET [8] and MAST [9, 10] have demonstrated that the application of resonant magnetic perturbation is able to mitigate or suppress ELMs while keeping sufficient confinement properties. The limits of the process, in terms of operation domain, are not yet accurately known, DIII-D being up to now the only Tokamak where a complete suppression of ELMs has successfully been obtained. In addition, experiments in different Tokamaks reveal opposite results for similar conditions, for example RMP can trigger ELMs during ELM-free phases in NSTX [11] and COMPASS [12]. With that respect, TCV unique plasma shaping and positioning capability could extend the range of accessible magnetic perturbation modes for a given RMP coil system geometry and contribute to a clearer description of the conditions required for ELM suppression.

Error fields are another aspect of toroidally asymmetric magnetic fields. They are created by construction tolerances in Tokamak coil positions and shapes. These fields, dominated by low values of the toroidal mode number, induce plasma braking and locked modes [13], themselves responsible for disruptions. Their effects can be corrected by applying an asymmetric field of opposite sign, as provided by a SCS. Measurements have shown that these fields are non negligible on TCV and that their correction could be beneficial to the operation of the machine.

Vertical control is required to stabilize the highly unstable vertical position of the plasma. It is obtained by applying an axisymmetric radial magnetic field. The growth rate of vertical modes is such that the vertical control coils need to be located inside the Tokamak vessel to avoid screening of the control field. TCV already has a vertical control system, namely the internal G-coils. Due to the lack of free space inside the vessel and to the required number of feedthroughs, it would be difficult to have both a new SCS and the actual internal coil systems coexisting in the machine. Therefore, the G-coils must be removed and the SCS must be designed to provide the vertical control functionality.

Generally, stationary asymmetric magnetic fields result in a toroidal plasma

braking, as observed in the case of strong error fields. For higher toroidal harmonics, perturbation fields can also lead to counter-current toroidal acceleration, as reported recently on DIII-D [14, 15, 16]. This effect could be of particular interest for TCV, since there is presently no external source of momentum on the machine, due to the absence of NBI heating.

Tearing modes [17, 18] are regularly present in Tokamaks. In TCV, their frequency is typically in the range of 5 kHz. A SCS powered with a high bandwidth source could, taking into account the vessel screening, open a field of research on the interaction of these modes with rotating perturbations, especially on the question of stability and phase locking of the modes.

Resistive wall modes [19, 20] (**RWM**) are ideal MHD instabilities that are not stabilized by the vessel wall because their growth rate is slower than the resistive time of the vessel. A SCS covering a sufficient portion of the wall could be used as a way to actively reproduce the wall screening on slower time scales, following the smart shell principle [21] demonstrated on RFX [22].

In this document, a description and a characterization of two proposed SCS designs, namely the in-vessel and ex-vessel SCS, are given. The physical arguments at the root of the proposed designs are detailed in section 2, where the geometry of the designs, the current requirement for RMP and the expected perturbation spectra and ergodization features are also presented. The spectral characterization of the designs is given in section 3. The study on error field control (**EFC**) is presented in section 4, including the determination of the current requirement for the error field correction on TCV. The questions of inductance and wall coupling are dealt with in section 5. This section also details the determination of the SCS response function. The requirements for vertical control are established in section 6 using a principle of equivalence with the system currently used on TCV. The voltage and current induced in the in-vessel SCS during a plasma disruption are calculated in section 7. The maximal magnetic force exerted on the SCS is calculated in section 8. A discussion on the impact of the number of turns per coil and a scaling of different parameters with this parameter are presented in section 9. The issue of coil heating due to Joule effect and the questions of cooling time and necessity of active cooling are addressed in section 10. The document ends with a short conclusion on the presented studies. Note that the ex-vessel design has been studied for a limited number of aspects, namely RMP, EFC and self-inductance.

2. RMP and coil system design

This section first describes the principle of RMP. This includes the description of the method used to establish the current requirements and the approaches used to qualify a SCS with respect to RMP. Physical arguments are then given to optimize the coil system topology in terms of poloidal coil location, poloidal and toroidal coil distribution, individual coil shape and dimensions, number of coils and toroidal phase shift between coil rows. Finally, two coil designs are proposed and discussed with respect to their expected performances, using vacuum field calculation in a number of situations.

2.1. Principle of RMP

The technique of resonant magnetic perturbation is based on the application of a magnetic perturbation perpendicular to the plasma equilibrium flux surfaces with a spatial variation tuned to align with the equilibrium magnetic field lines. This perturbation is generally created by a set of poloidally and toroidally distributed coils having mainly a radial field contribution. The current explanation of ELM mitigation or suppression by RMP is based on the overlap of the magnetic islands created by RMP that generates an ergodic zone in the plasma edge, itself increasing the outward transport and thereby limiting the pedestal gradients to values below the instability limits. This description is however still incomplete as the weak effect of RMP on the pedestal electron temperature remains unexplained.

The formalism used to describe RMP [23, 24, 25] is based on a local normalization of the perpendicular component $B_\perp$ (with respect to magnetic flux surfaces) of the magnetic perturbation:

$$b(\rho, \theta^*, \phi) = \frac{B_\perp R \|\nabla \rho\|}{B_{0,\phi}} \tag{1}$$

where ρ is a flux surface label, θ^* is a poloidal angle coordinate defined such that equilibrium field lines are straight in the (θ^*, ϕ) plane, ϕ is the toroidal angle, R is the major radius and $B_{0,\phi}$ is the toroidal component of the equilibrium field. The amplitude of the resonant components of the perturbation is given by the space Fourier transform of b along the angular coordinates:

$$\tilde{b}(\rho, m, n) = \frac{1}{(2\pi)^2} \iint_0^{2\pi} \mathrm{d}\phi \mathrm{d}\theta^* b(\rho, \theta^*, \phi) \mathrm{e}^{\mathrm{i}(-m\theta^* - n\phi)} \tag{2}$$

The width of the resulting island on the resonant surface ρ_s is then given by:

$$\Delta\rho = 4\sqrt{\frac{2|\tilde{b}(\rho_s, m, n)|q_s^2}{\mid mq_s' \mid}} \tag{3}$$

where $q_s = m/n$ is the value of the safety factor at ρ_s and q_s' is the derivative with respect to ρ.

Note: Since the RMP coil systems are generally made of saddle-shaped coils, the generic name of saddle coil system (SCS) will be used in the remaining part of this document.

2.1.1. Current requirement determination

The determination of the minimal required current for RMP is based on two complementary approaches. In the first approach, the required perturbation amplitude is given by the condition of creating a radial magnetic field at the plasma separatrix that has the same amplitude, with respect to the toroidal field, as in DIII-D or JET. This condition corresponds to a perturbation of 0.4%, i.e. 5.7 mT for TCV. The second approach is based on the criterion of magnetic island overlap in the plasma edge. According to Fenstermacher [26], the ergodization of the plasma edge on a width of $\Delta\psi_{01} = 0.17$ is required to suppress ELMs on DIII-D, where ψ_{01} is the normalized poloidal flux. Magnetic island overlap is quantified by the Chirikov parameter $\sigma(\psi_{01})$ [25] and ergodization appears when the condition $\sigma > 1$ is satisfied. The value of σ is a function of the amplitude of the current in the SCS and the required current can therefore be calculated using the condition $\sigma(0.83 \leq \psi_{01} \leq 1) \geq 1$.

2.1.2. Qualifying a SCS with respect to RMP

For a given plasma equilibrium, the magnetic perturbation created by a SCS can be characterized by the space spectrum $\tilde{b}(\rho, m, n)$. In the case of RMP, the spectrum of the magnetic perturbation must be optimized to obtain minimal resonant core mode amplitudes, maximal edge ergodization and minimal non resonant mode amplitudes, while maintaining technically realistic coil current requirements [27, 28, 14, 15, 16]. Using independent coil powering gives a certain freedom with that respect. A method [25] has been developed to calculate the optimal coil current distribution for a given coil setup and plasma equilibrium and quantify the quality of the obtained perturbation spectrum. The method is based on a Lagrange optimization

where a cost function is minimized while a given amplitude is imposed for a set of modes. For well-behaved cases of RMP, the cost function f is defined as:

$$f(\{I_c\}) = \frac{1}{N_{coils}} \sum_c I_c^2 + w_g f_g(\{I_c\}) \tag{4}$$

where $\{I_c\}$ are the coil currents, N_{coils} is the number of coils, f_g is the integral of $|\tilde{b}|^2$ over the whole space and w_g is a tuning weight. Minimizing f_g results in spectrum optimization because it corresponds to peaking the spectrum around the resonant edge modes, for which an imposed amplitude is used. f is hence made of two parts, current minimization and spectrum optimization, with a weight w_g used to adjust their relative importance. The quality of the obtained spectrum is then quantified with a figure of merit r defined as the ratio of the amplitude of a resonant edge mode to f_g and therefore measuring the degree of peaking of the spectrum around the resonant edge modes.

Once the optimal current distribution is known, the proposed SCS is qualified with respect to a variety of elements:

Spectrum quality: a figure of merit is attributed to the optimal spectra obtained for each controlled value of the toroidal mode number n of the perturbation. An equivalent figure of merit is also attributed to the spectra corresponding to a minimal current requirement while maintaining a certain activation of the edge modes.

Ergodization localization: by plotting the location of the generated islands as a function of the SCS current and the flux surface coordinate on a 2D map, the localization of the ergodized regions can be visualized. This method of analysis is similar to a radial profile of the Chirikov parameter but solves the issue of island pairing inherent to the Chirikov approach.

Poincaré plots: the vacuum magnetic field perturbation is added to the equilibrium field and a large number of field lines are followed in space. A Poincaré plot is obtained by marking the position of the field lines on a poloidal cross-section after each toroidal turn. They provide an independent way of determining the location of the ergodized regions. Although they require a much longer computation time than the previous method, the obtained result is more robust since they require less intermediate computations and do not assume a constant perturbation amplitude across the islands.

2.2. Optimal coil system topology

In order to limit the range of studied coil systems, it is useful to formulate a number of generic arguments serving as reflection guides. These arguments are then used to propose a number of possible SCS designs, which are in turn qualified with respect to a given plasma equilibrium using the methods described above.

2.2.1. Toroidal distribution

As far as RMP is concerned, there is no theoretical constraint on the toroidal distribution of coils in the coil setup. However, a number of arguments must be considered:

- A system that is not evenly-spaced toroidally activates a whole family of toroidal modes, with few control on the relative amplitudes in each value of the toroidal mode number n, although the perturbation spectrum is usually peaked on modes with low n values. This may seriously impair the experimental usage of the coil system, as well as the physical interpretation of the experimental results. For example, it becomes very difficult to limit the magnetic field line ergodization to the plasma edge in such a case.

- A coil system can therefore be used for error field correction only if it is evenly-spaced toroidally.

- In vertical control operation, the pure $n = 0$ correction is much better mimicked if the coils cover the whole toroidal circumference, i.e. if they are juxtaposed with one another.

- If the coils are juxtaposed with one another and evenly-spaced, the toroidal spectrum of the perturbation displays less activation of sideband modes. It also means that the coil current requirements to obtain a given perturbation amplitude are smaller.

The optimal toroidal distribution is therefore made of evenly-spaced juxtaposed coils.

2.2.2. Poloidal location and distribution

Concerning the poloidal location and distribution of the coil system, the following arguments should be considered (see [29] and equation (1)):

- Since the edge safety factor is usually large in Tokamaks, a perturbation must activate modes with high values of the poloidal mode number m in order to be resonant. Sharp poloidal variations of the magnetic perturbation are therefore necessary. This constraint can be somewhat lessened on the low field side since the poloidal angle between two successive turns of a field line is larger in that particular location.

- A magnetic perturbation located close to a region of the plasma where the poloidal flux expansion is small has a larger effect. Since Tokamak plasmas are vertically elongated, such a region is present on the median plane of the plasma. In addition, the flux expansion is further reduced by the Shafranov shift on the low field side of the machine.

- The relatively smaller toroidal magnetic field on the low field side contribute to a larger effect of a magnetic perturbation located there.

From these arguments, it appears clearly that the coil system must be located on the low field side of the machine, spread on as many rows as possible.

2.2.3. Individual coil shape and dimension

The exact shape of each coil has small significance in terms of perturbation spectrum. A saddle-like shape is nonetheless preferred to other possible shapes since it maximizes the amplitude of the perturbation field for a given coil area and, in case of juxtaposed coil systems, minimizes the effect of spatial discretization when the coils are combined to mimic systems having smaller spatial mode numbers. In a system made of juxtaposed coils, the coil dimension is determined by the poloidal and toroidal number of coils. Otherwise, the coils should be as large as possible to minimize the current requirement.

2.2.4. Number of coils

The number of coil rows is determined as a trade-off between current requirements and spectrum shaping. A higher number of rows allow more control on modes with high values of m, but comes with smaller coils requiring more current. The number of coils in the toroidal direction, $N_{coils,t}$, defines n_{max} the highest controllable value of n. Again, a trade-off between current requirements and coil system features must be chosen. Important aspects in this matter are the number of available feedthroughs, the cost of power supplies and the natural geometry of the Tokamak.

2.2.5. Mechanical toroidal phase shift between coil rows

When using independent coil powering, the phase of the perturbation created by each row of coils can be tuned for all the values of n smaller than n_{max}. In the case where $N_{coils,t}$ is even and for $n = n_{max}$, this statement does not hold and the spectrum of the perturbation can only be optimized by adjusting the relative current amplitude between coil rows, which might be insufficient. In that case, the alignment of the magnetic perturbation with the magnetic field lines in the edge of the plasma may be optimized by a mechanical toroidal phase shift between coil rows. Such a design raises a number of issues:

- The optimization is rigid and might be optimal with respect to a narrow experimental domain, in particular limited by the value of q_{edge}, the sign of the helicity, the plasma position and the plasma shape.

- The optimization rigidity may be alleviated by increasing the number of coils on one or more rows and changing the coil connections in these rows depending on the desired phase shift. However, such a solution requires a much higher number of coils and the development of multiple coil designs. Space occupation might also be an issue.

2.3. Optimal coil system topology for TCV

The particular geometry of TCV, approximately 3 rows of 16 evenly-spaced portholes, and the requirement of flexible plasma positioning dictate most of the topology choices for the SCS project. The positioning flexibility requires the conservation of the mid-plane symmetry of the machine. Since small elongation plasmas located in the top or bottom half of the machine are commonly created, a mid-plane coil row is also necessary. Therefore, at least (and at most, due the portholes) 3 coil rows must be installed. The choice of n_{max}, the highest controllable value of n, is driven by the toroidal symmetry of the machine: $n_{max} \in \{1; 2; 4; 8\}$. RMP requires at least $n_{max} = 2$, but $n_{max} = 4$ is certainly preferable to ensure a certain flexibility during experimental studies. $n_{max} = 8$ would not only represent an important cost, but also be less interesting in terms of resonant mode control since the corresponding values of m are too high with respect to the capabilities of a 3-row system.

Concerning the question of mechanical toroidal phase shift between coil rows, in a $n_{max} = 4$ design and taking the vessel geometry into account,

only a $2\pi/16$ phase shift of the mid-plane row would be sensible. For $n = 4$, such a phase shift actually worsen the magnetic perturbation alignment since the field line pitch angle is usually much flatter than the pitch angle of the perturbation that would then be created.

Following the arguments stated above, the optimal coil system topology for TCV consists in 3 rows of 8 evenly-spaced coils. If possible, these coils should be juxtaposed with one another and the rows should be vertically aligned.

2.3.1. In-vessel coil system

An in-vessel coil system would be the most interesting option in terms of potential experimental usage of the system since all the intended applications would be possible. A number of important restrictions are nonetheless present for such a system, as shown in the list below:

- The coils must be passed through the manhole during the installation procedure. As a result:
  - The toroidal extent of the coils is limited by the height of the vessel. This is compatible with a choice $n_{max} = 4$, i.e. a coil encircling 2 portholes.
  - The height of the coil is limited by the diameter of the manhole, giving a final height of approximately 38 cm.
- The number of portholes for feedthroughs limits the number of coils ($n_{max} \leq 4$).
- The coils must be as thin as possible to fit in a narrow space between the vessel and the tiles.
- The coils must be as far away as possible from the vessel to limit the screening of the perturbation and as close as possible to the plasma in order to minimize the required coil current and maximize the amplitude of modes with high values of m.
- The coil support must be strong enough to endure the mechanical shocks related to plasma disruptions.
- The coil design must be vacuum-compatible.

- The coil design must account for the coil temperature increase due to Joule effect in the absence of active cooling and due to vessel baking during conditioning phases.

A possible design is shown in figure 1. This design is compatible with all the requirements stated above and follows the optimization guidelines. The 10-turn design used for numerical applications throughout this document is shown in figures 2 and 3.

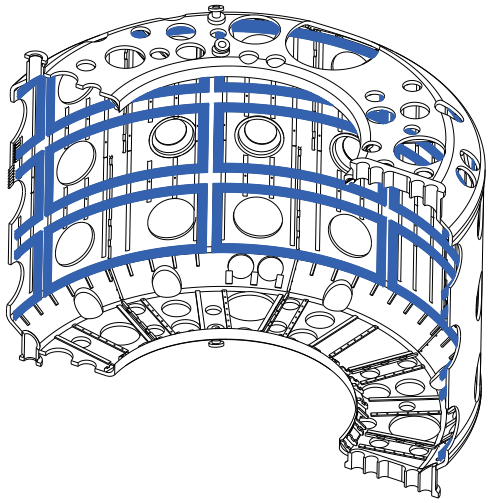

Figure 1: Perspective view of the optimal in-vessel design for the SCS project (in blue) for TCV, drawn on top of the vacuum vessel (in black). The system consists of 3 rows of 8 internal saddle coils located on the low field side of the torus. The coils are toroidally juxtaposed and vertically aligned. The number of turns per coil in the figure is illustrative only.

2.3.2. Ex-vessel coil system

An ex-vessel coil system might prove interesting in terms of cost reduction. The restrictions specifically related to an ex-vessel system are listed below:

- The vertical control and mode rotation control features are lost due to the vessel wall screening of any high frequency perturbation. Resistive wall mode control becomes very limited or impossible.

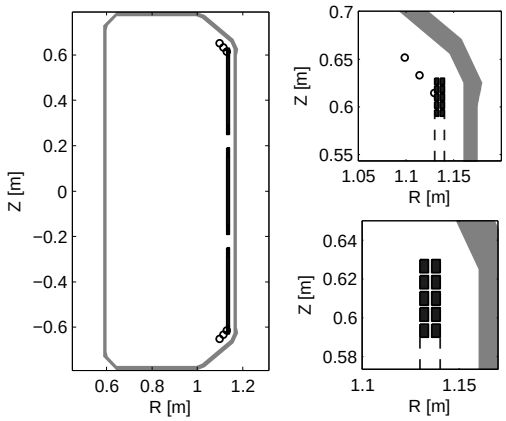

Figure 2: Poloidal cross-section of the 10-turn in-vessel SCS design. On the LHS, the toroidal projection of the coils is shown, as well as the actual position of the internal fast coils, also known as G-coils (○). On the RHS, a zoom on the coil is shown.

- The coils are further away from the plasma. As a result, the amplitude of modes with high values of m is decreased, with a possible detrimental effect on ELM control by RMP, and the current requirement is increased.
- The current induced in the coils due to a disruption is reduced, thanks to the vessel wall screening.
- The space occupation outside the vessel limits considerably the possible coil geometry. A "chair-like" design might be envisaged to minimize the distance between the coils and the plasma. The toroidal juxtaposition of coils is not possible in that case.

A possible design is shown in figure 4. The design is compatible with the restrictions stated above but some portholes might need to be re-engineered in order to accommodate such a system. A configuration with only 4 coils toroidally, generating a perturbation with $n_{max} = 2$, would fit more easily into the current TCV setup. The single-turn design used for numerical applications throughout this document is shown in figures 5 and 6.

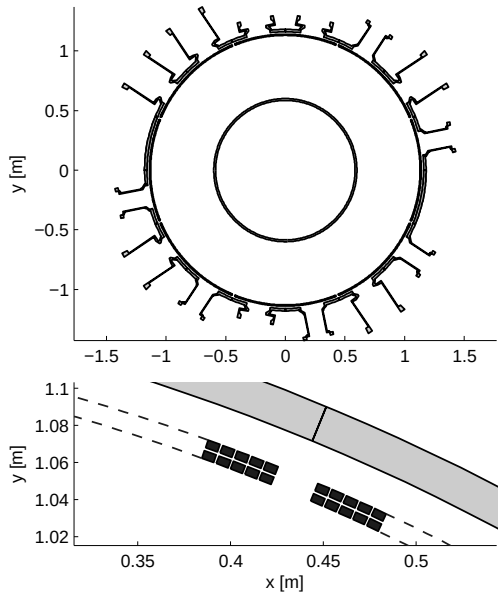

Figure 3: Toroidal cross-section of the 10-turn in-vessel SCS design. Top: overview of the TCV vessel with the coil array (nearly continuous circle). Bottom: zoom on a particular pair of coils. NB: the tangential porthole is missing on the figure.

2.4. RMP performances and current requirement of the in/ex-vessel SCS

In this section, the performances of the proposed in- and ex-vessel SCS in terms of RMP are assessed following the principles given in section 2.1.2. The current requirements (see section 2.1.1) are also given.

2.4.1. Equilibrium description

A typical ELMy H-mode plasma equilibrium is used to calculate the different parameters used in the design quality assessment. The same equilibrium is used at two different vertical positions of the magnetic axis: $z_{mag} = 0$ and $z_{mag} = 0.23\,\mathrm{cm}$. The plasma is characterized by a density on axis $n_e = 7.5 \cdot 10^{19}\,\mathrm{m}^{-3}$, a plasma current $I_p = 415\,\mathrm{kA}$, a toroidal magnetic field on axis $B_{\phi,axis} = 1.4\,\mathrm{T}$, a major radius $R_{axis} = 0.91\,\mathrm{m}$, a minor radius $a = 0.22\,\mathrm{m}$, a triangularity $\delta_{95} = 0.4$, an elongation $\kappa_{95} = 1.7$, a normalized pressure $\beta_p = 0.65$ and a safety factor $q_{95} = 2.6$.

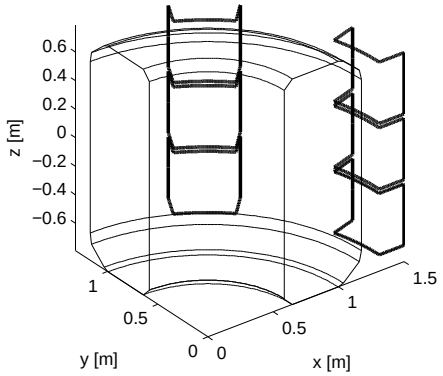

Figure 4: Perspective view of the optimal ex-vessel design for the SCS project for TCV, drawn on top of the vacuum vessel. The system consists of 3 rows of 8 external saddle coils located on the low field side of the torus. The coils are vertically aligned.

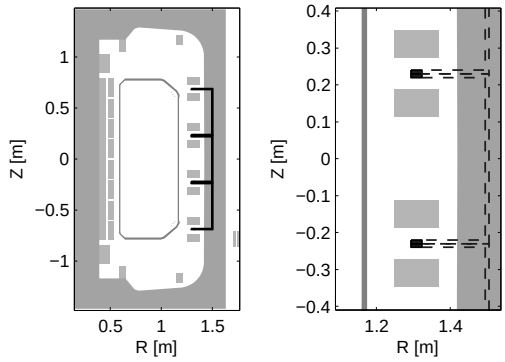

Figure 5: Poloidal cross-section of the ex-vessel SCS design. On the LHS, the toroidal projection of the coils is shown, as well as the position of the TCV coil system. On the RHS, a zoom on the coil is shown.

2.4.2. Current requirements and figure of merit

The figure of merit and the required current, based on the overlap of magnetic islands, are shown in figure 7 for both coil designs and $z_{mag} = 0$. Both parameters are shown as a function of the cost function weight w_g indicating a scan between the current requirement minimization and the

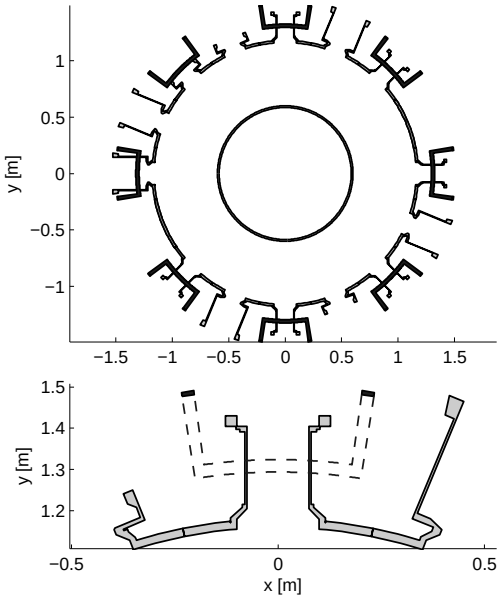

Figure 6: Toroidal cross-section of the ex-vessel SCS design. Top: overview of the TCV vessel with the coil array. Bottom: zoom on a particular coil. NB: the tangential porthole is missing on the figure.

spectrum optimization.

The general aspects of the dependence of the figure of merit and the required current on the weight w_g are discussed in [25]. The focus is brought here on the comparison between both designs. Despite the extra distance to the plasma, the ex-vessel design displays spectral features close to the values given by the in-vessel system. However, in the case of the in-vessel SCS, a realistic multi-turn coil design has been used to calculate the spectra, whereas a single-turn design has been used for the ex-vessel system. This choice might have a noticeable impact on the presented results, since a multi-turn system produces a perturbation with less activation of the modes with high values of m. As expected, the current requirements for the ex-vessel system are much larger than those for the in-vessel system. This result is explained by the limited toroidal extent and the larger distance to the plasma in the ex-vessel case. The figure of merit r generally takes a higher value at $z_{mag} = 0.23$ for w_g small. At this position, the location of the transition from the equatorial coil row to the upper coil row coincides with the plasma magnetic axis and

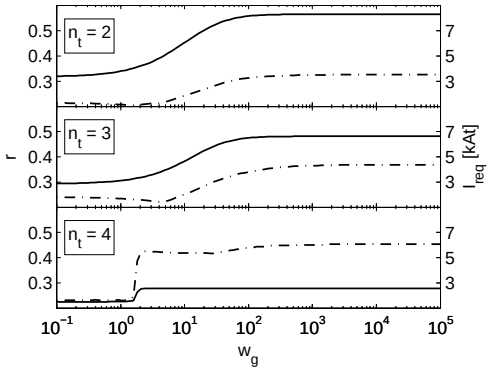

(a) In-vessel design

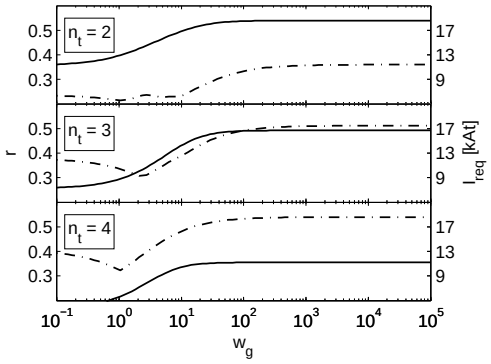

(b) Ex-vessel design

Figure 7: Figure of merit r (solid lines) and required current for edge ergodization I_{req} (dashed-dotted lines) as a function of the weight w_g in the cases $n_t = 2$, $n_t = 3$ and $n_t = 4$ for the in- and ex-vessel SCS and $z_{mag} = 0$.

the SCS therefore naturally produces perturbations with high values of m without increasing the value of the current cost function. However, the overall current requirements are higher (factor 2 to 3) at $z_{mag} = 0.23$, especially for optimal spectra. This is due to the weak contribution of the bottom coil row.

As shown in figure 7, the current requirements based on magnetic island overlap vary greatly as a function of the degree of optimization of the spectra. A study published in [25] also shows that they depend on the equilibrium parameters, mainly the q-profile. To determine the DIII-D and JET equivalent current, the relative current distribution giving an optimal spectrum at $z_{mag} = 0$ has been retained. This choice is justified by a too weak activation of the bottom and top coil rows in the minimal current configuration leading to a nearly insignificant contribution to the total perturbation in that case. For the in-vessel system, a DIII-D and JET equivalent is given by a current of approximately 4 kAt. As shown in figure 7, such a current would be sufficient for non-optimal spectra. At $z_{mag} = 0$, the reserve of current dedicated to the error field correction (approximately 3 kAt) could be used to reach the optimal spectra. Note that at $z_{mag} = 0.23$, the optima would not be reached unless the current limit for RMP only is increased to 12 kAt. For the ex-vessel system, the DIII-D and JET equivalent is reached for a current of 14 kAt. As before, the error field correction current can be used for RMP and offers an additional 7 kAt. Here again, the optimal spectra at $z_{mag} = 0.23$ are reachable only at the cost of a large increase of the current requirement for RMP.

2.4.3. Spectra

The magnetic perturbation spectra corresponding to both extremes of w_g for the in-vessel SCS design, $n = 2$ and $z_{mag} = 0$ are plotted in figure 8 to illustrate the process of spectrum optimization. This detailed view shows that the figure of merit captures correctly the main features of the spectra. In general, the $z_{mag} = 0$ spectra of the in-vessel system exhibit sharper variations along m than those of the ex-vessel system, consistently with the smaller distance to the plasma of the in-vessel system. For all cases, the alignment of the perturbation with the q-profile is sufficient and the optimization of the spectra is efficient, particularly in terms of reduction of core mode amplitudes.

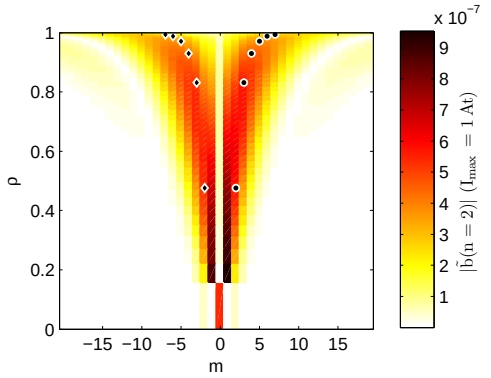

(a) Minimal current

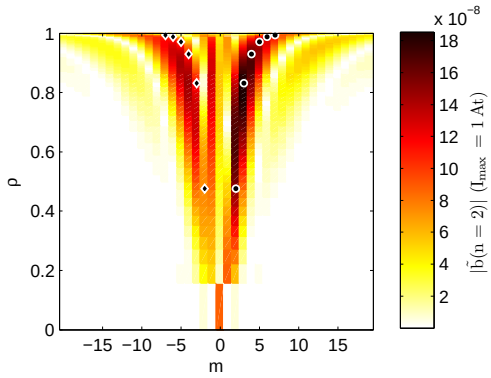

(b) Optimal spectrum

Figure 8: $\left|\tilde{b}(\rho, m, n = 2)\right|$. ●: resonant flux surface locations, ◆: symmetrical non resonant counterparts. Case: in-vessel, $z_{mag} = 0$, $n = 2$.

2.4.4. Ergodization map and Poincaré plot

An example of ergodization map is given in figure 9. This corresponds to the in-vessel design with a current distribution giving an optimal spectrum for $n = 4$ and $z_{mag} = 0$. The maximal current in the plot is given by the condition of equivalence with DIII-D and JET perturbation amplitude at the separatrix. In that case, the ergodization layer is well located at the edge of the plasma and grows toward the core as the current is increased.

Although Poincaré plots are not directly used in the design study, they provide a point of comparison to verify the results obtained by the analytical island width approach. Indeed, the only common part to both approaches

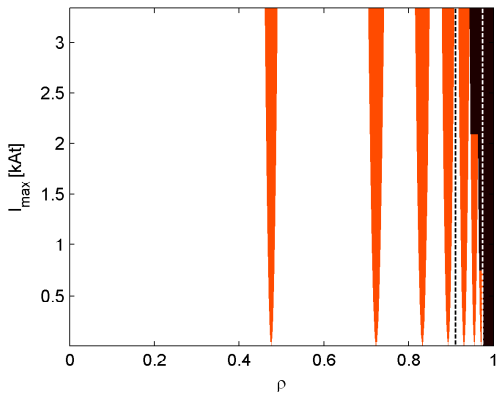

Figure 9: Ergodization map. Island width (red) and ergodic regions (dark brown) shown as a function of the maximal current fed in the SCS. Vertical black dashed line: inner limit of the required ergodic zone according to the $\psi_{01} = 0.83$ limit. Vertical white dashed line: $\psi_{01} = 0.95$. Case: in-vessel, $z_{mag} = 0$, $n = 4$, optimized spectrum.

is the total magnetic field in cylindrical coordinates. The Poincaré plot corresponding to figure 9 is shown in figure 10. The edge ergodization and the isolated core islands can be observed. In addition, the deformation of the plasma separatrix due to the magnetic perturbation is clearly visible. Figure 10a illustrates the effect of strike point splitting due to the application of RMP. Interestingly, the simple vacuum field approximation is sufficient to account for an experimentally observed phenomenon [30, 31, 32, 33].

3. Spectral characterization of the SCS

The spectrum of the magnetic field perturbation as defined in (2) is a function of the coil geometry, the coil locations and the relative coil currents. Due to the small number of coils and to their identical geometry, spectral degeneracy occurs, consequently limiting the number of simultaneously controlled modes provided by the coil system. A simple theory [25], based on the combination of the real-space Fourier transform of the perturbation due to a single coil and the current-space Fourier transform of the current distribution of a set of equivalent coils, is used to entirely characterize the spectral limitations of a coil system. Formally, the Fourier transform $\tilde{b}$ of the magnetic perturbation is expanded using sets s of toroidally equivalent coils (e.g.

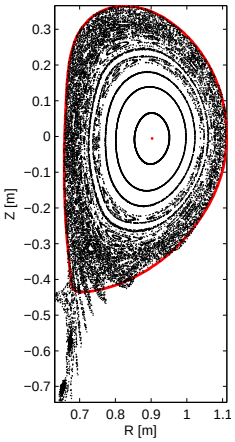

(a) Poloidal cross-section

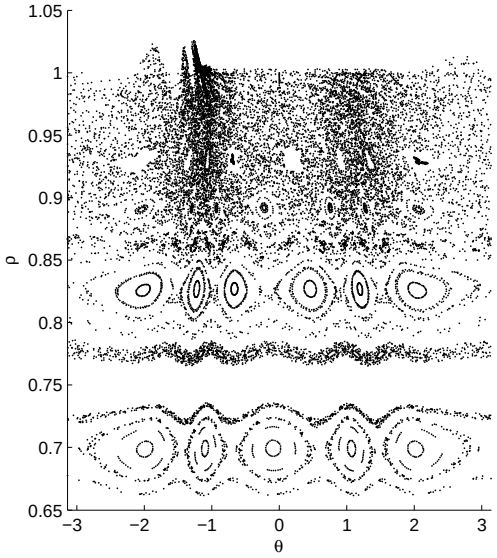

(b) Flux coordinates

Figure 10: Poincaré plot of the magnetic field lines for the in-vessel SCS design in the $n = 4$ configuration with optimized spectrum, using the $z_{mag} = 0$ equilibrium. The SCS is powered so that the Chirikov criterion is satisfied. The equilibrium separatrix and magnetic axis are shown in red. Core islands are not represented.

identical coils on the same row, with arbitrary toroidal spacing ϕ_c^s):

$$\begin{aligned}\tilde{b}(\rho,m,n) &= \sum_s \sum_c \tilde{b}_c^s(\rho,m,n) I_c^s \\ &= \sum_s \tilde{b}_0^s(\rho,m,n) \sum_c I_c^s \mathrm{e}^{-\mathrm{i}n\phi_c^s} \\ &= \sum_s \tilde{b}_0^s(\rho,m,n) \hat{I}^s(n) \end{aligned} \tag{5}$$

where $\tilde{b}_c^s$ is the Fourier transform of the magnetic perturbation due to a unit current in coil c of set s, the index 0 labels a reference coil in the set having $\phi_0 = 0$ and $\hat{I}^s$ is the generalised discrete Fourier transform of I_c^s in the current space. In the case of evenly spaced coils, $\hat{I}^s$ is equal to the standard discrete Fourier transform of I_c^s, so that modes with different values of n can be orthogonally activated by using Fourier modes for the currents in each coil row. In addition, the equalities $\hat{I}^s(n + pN_s) = \hat{I}^s(n)\ \forall p \in \mathbb{N}$ and $\hat{I}^s(N_s - n) = \hat{I}^{s*}(n)$ where N_s is the number of coils in the set s mean that the activation of modes with a given value of n implies the activation of a whole class of modes with other degenerated values of n.

In the particular topology proposed for TCV (section 2.3), equation (5) leads to the conclusion that 5 orthogonal classes of n are available $\{0;\ 1;\ 2;\ 3;\ 4\}$, with main degenerate pairs $\{0;\ 8\}$, $\{1;\ 7\}$, $\{2;\ 6\}$ and $\{3;\ 5\}$. For classes $n = 1$, $n = 2$ and $n = 3$, the 3 coil rows allow a maximum of 3 simultaneous targets (i.e. 3 points (ρ, m, n) for which $\tilde{b}$ is controlled) per class, while for classes $n = 0$ and $n = 4$, only 1 target per class is allowed (with simultaneous spectrum optimization if independent power supplies are used). The toroidal periodicity results in maximal gains for each row as follows: $g(\{0;4\}) = 8$, $g(\{1;3\}) = 4.3$ and $g(\{2\}) = 5.6$, where g is the gain of a perturbation amplitude for 8 coils with respect to the amplitude given by a single coil. For class 3, the degeneracy between $n = 3$ and $n = 5$ and the small spectral distance between these modes implies a non negligible effect of $n = 5$ modes when working in $n = 3$ configurations.

4. Error field correction

This section describes the issue of error fields on TCV and how the proposed SCS could correct them. First, the error field situation on TCV is described. Then, the correction principle used in this study is detailed and

the SCS design capabilities are discussed. Finally, the question of current requirement is addressed.

4.1. Error field on TCV

According to Piras [34], the main source of non-axisymmetric error field on TCV is a tilt of the central coil column corresponding to a misalignment of a maximum of 5 mm of the poloidal field coils located on the central column. This shift corresponds to a $n = 1$ radial perturbation in the range of 1 to 5 mT. The effect of the error field on the plasma is a function of the powering of the different poloidal coils and also a function of the distance between the coils and the plasma.

4.2. Error field correction principle

A correction of the error field by a SCS in the entire vacuum chamber is not possible. The SCS can only correct a few spectral components of the error field on a given number of flux surfaces. If the source of error field is known, the resulting magnetic perturbation on the flux surfaces can be calculated for a given magnetic equilibrium. The simplest approach consists in assuming no plasma response to the error field and using the vacuum error field as the error field existing at the flux surfaces. A possible theoretical approach [24] for EFC consists in using a SCS to create a magnetic perturbation that cancels out the most damaging components on the resonant flux surfaces (e.g. cancelling out the $(n, m) = (1, 2)$ component on the $q = 2$ surface). Of course, the SCS will itself be a source of error field and its own contribution should be minimized. A more advanced theoretical approach [35, 36], taking into account the amplification of certain components of the error field by the plasma, would possibly give more accurate results, but since the aim here is only to estimate the required current for EFC, the simple vacuum field approach described above is thought to be sufficient.

The experimental approach consists in scanning the parameter space of the $n = 1$ perturbation created by the SCS and correlating the scans with the plasma performances or breakdown robustness. If the number of degrees of freedom of the SCS is large, such an approach might prove extremely resource consuming, especially if the variety of possible magnetic configurations is large, like on TCV.

4.3. EFC capabilities with the proposed SCS

Since error field is mainly present for $n = 1$ components, EFC can be obtained independently of other usages of the SCS as long as the combined current requirements do not exceed the design value. As described in section 3, the proposed SCS can correct at most 3 modes. Instead of a total correction of 3 modes, the SCS can also be fed with a current distribution that minimizes the error field on a larger number of modes, without cancelling them totally. Depending on the experimental program, one could for example correct exactly a particularly strong resonant mode and minimize the amplitude of a set of non-resonant modes. The method described in [25] returns the optimal current distribution for any of the options described above.

4.4. Required current for EFC on TCV

In order to determine the required current for EFC on TCV, the $n = 1$ error field due to a 5 mm radial shift of each poloidal field coil powered at their nominal current of 7.5 kA is calculated on the main resonant flux surfaces $q = 1$ and $q = 2$ of both magnetic equilibria described in section 2.4.1. The SCS current distribution is then optimized to cancel this field in different situations: cancellation of the $m = 1$ or $m = 2$ resonant mode only, simultaneous cancellation of both components and, finally, cancellation of one of the resonant modes while minimizing the activation of parasitic modes by the SCS. In all cases, the results are given for the error field phase requiring the largest coil current.

The results for the in-vessel SCS are given in table 1a. As expected, the coils that are close to the magnetic axis have a larger effect. The error fields created by the so-called F-coils (low field side poloidal coils) also have a larger impact than those created by the E-coils (high field side poloidal coils), consistently with the expected larger impact of perturbation coils located on the low field side of the vessel (see section 2.2.2). The required current depends strongly on the case under consideration. In the present study, a variation from 0.9 to 16.2 kAt is observed. Following the conclusions of the study of the required current for RMP, the required current for EFC increases when an optimal spectrum is required or when several modes are corrected simultaneously. The situation becomes worse when the plasma is located at $z_{mag} = 0.23$ and any of both previously stated situations occurs. When considering the values given in table 1a, it seems reasonable to fix the required current at $I_{req,in} = 3$ kAt since the error field is mainly created by

the E-coils in TCV and since special correction scenarios (i.e. multi-mode or optimal spectrum approaches) could use the reserve of current dedicated to RMP (4 kAt in this case). With such a choice, the current limit would be sufficient to cover the standard correction scenario (i.e. one mode with minimal current) with sufficient margin in all the cases and the second limit offered by the RMP reserve would give access to most of the cases of interest. Only multi-mode correction at $z_{mag} = 0.23$ would not be possible, but such a scenario would require 9 kAt in addition to the RMP reserve and therefore represent a large increase of cost with respect to the expected scientific output.

The results for the ex-vessel SCS are given in table 1b. Observations similar to those given for the in-vessel case could be mentioned. Following the arguments given for the in-vessel case, the required current for EFC can be fixed at 7 kAt (recall: the required current for RMP is 14 kAt in that case).

5. Inductance, wall currents and response function of the SCS

The electrical characterization of the SCS requires the calculation of the self and mutual inductances of the coils. For in-vessel coil systems, the electrical coupling of the coils with the vessel wall must also be characterized in order to deduce the frequency response of the coil system and the proportion of screening due to the wall. These aspects are studied in this section.

5.1. Mutual and self inductance

The mutual and self inductance calculation of the SCS is based on the Neumann's formula (A.1). When possible, analytical or semi-analytical formulations are used to speed up the calculation. The details of this procedure are given in Appendix A.

5.2. Calculation results in DC mode

When the coils are powered with a constant current, the presence of the vessel wall has no importance. In that case, the coils of the in-vessel design, in a 10-turn configuration, have a self-inductance of 138 μH while the coils of the ex-vessel design, in a single turn configuration, have a self-inductance of 1.44 μH. For the in-vessel design, the mutual inductance between direct neighbours on the same row is of -6 μH and between direct neighbours one row apart of -10.6 μH. The current induced in a coil due to the powering of a

m	z_{mag} [m]	Optimal spectrum	max($I_{req,\,E}$) [kAt]	max($I_{req,\,F}$) [kAt]
1	0	No	0.9 (E3)	1.3 (F5)
1	0	Yes	1.7 (E3)	2.5 (F5)
2	0	No	1.3 (E4)	1.3 (F4)
2	0	Yes	1.7 (E4)	1.8 (F4)
[1,2]	0	No	6.5 (E4)	7.7 (F4)
1	0.23	No	0.9 (E5)	1.3 (F6)
1	0.23	Yes	3.8 (E5)	5.7 (F6)
2	0.23	No	1.1 (E5)	1.2 (F5)
2	0.23	Yes	5.7 (E5)	6.5 (F5)
[1,2]	0.23	No	13.0 (E5)	16.2 (F6)

(a) In-vessel SCS

m	z_{mag} [m]	Optimal spectrum	max($I_{req,\,E}$) [kAt]	max($I_{req,\,F}$) [kAt]
1	0	No	3.2 (E3)	4.8 (F5)
1	0	Yes	4.1 (E3)	6.3 (F5)
2	0	No	4.4 (E4)	4.6 (F4)
2	0	Yes	5.1 (E4)	5.2 (F4)
[1,2]	0	No	24.9 (E4)	29.6 (F4)
1	0.23	No	2.9 (E5)	4.2 (F6)
1	0.23	Yes	8.5 (E5)	12.6 (F6)
2	0.23	No	4.0 (E5)	4.5 (F5)
2	0.23	Yes	13.7 (E5)	15.6 (F5)
[1,2]	0.23	No	26.9 (E5)	33.2 (F5)

(b) Ex-vessel SCS

Table 1: Required current for EFC with the in- and ex-vessel SCS. The "optimal spectrum" column mentions whether the required current is minimized ("No") or the parasitic modes are minimized ("Yes"). The maximal correction current for each group of poloidal coils is given. The coil for which this current is required is given in brackets. The E-coils are the high field side poloidal coils and the F-coils the low field side ones. Both sets are numbered from 1 to 8 from bottom to top (see figure 5).

neighbouring coil is therefore more than an order of magnitude smaller than the current in the active coil. The mutual inductance between coils located further apart is negligible.

5.3. Calculation of wall currents

In order to estimate the electromagnetic coupling between the vessel wall and the SCS, the wall is represented by a set of conducting filaments having an imposed geometry. The choice of filament geometry is determined by the expected spatial distribution of the vessel current density, which is in general conforming with the shape of the coils. Particular geometries are proposed below (sections 5.3.1 and 5.3.2). For the moment, it is sufficient to consider a set of generic vessel filaments. The electromagnetic system formed by the SCS and the wall is then completely described by the resistance and the self and mutual inductances of all the vessel filaments and coil turns. Assuming the time-dependence of the SCS currents to be $\mathbf{I_c}e^{\mathrm{i}\omega t}$, the wall currents are given by the vessel filament voltage equations:

$$[\mathrm{i}\omega\mathbf{M_{vv}} + \mathbf{R_{vv}}] \cdot \mathbf{I_v} = -\mathrm{i}\omega\mathbf{M_{vc}} \cdot \mathbf{I_c} \quad (6)$$

$$R_{ij} := R_i\delta_{ij} \quad (7)$$

$$R_i := \rho_{\mathrm{vessel}}\frac{l_i}{S_i} \quad (8)$$

with v the vessel filament index, c the SCS coil index, $\mathbf{I}$ the current vector, $\mathbf{R}$ the electrical resistance matrix, $\mathbf{M}$ the inductance matrix, l the conductor length, S the conductor cross-section and ρ the resistivity. As the frequency is increased, the image currents induced in the vessel wall reduce the magnetic flux created by the SCS and cancel partially the radial magnetic field perturbation. Above a certain frequency, the resistive contribution of the vessel filaments becomes negligible and the relative amplitude of the vessel currents saturates. In theory, the wall screening can therefore be completely compensated by increasing the value of the SCS nominal current, especially for the in-vessel design, but the necessary increase might be very large (a factor 5 to 10) depending on the distance between the coils and the vessel (see section 5.3.5).

The effect of the wall can be fully represented by an apparent inductance of the SCS. For this purpose, the SCS voltage equation must be used:

$$\mathbf{U_c} = \begin{bmatrix} (\mathrm{i}\omega\mathbf{M_{cc}} + \mathbf{R_{cc}}) & \mathrm{i}\omega\mathbf{M_{cv}} \end{bmatrix} \cdot \begin{bmatrix} \mathbf{I_c} \\ \mathbf{I_v} \end{bmatrix} \quad (9)$$

Using (6) to replace $\mathbf{I_v}$ in (9), the vessel contribution can be represented by a frequency-dependent apparent inductance matrix:

$$\mathbf{U_c} = [\mathrm{i}\omega \mathbf{M_{cc,app}}(\omega) + \mathbf{R_{cc}}] \cdot \mathbf{I_c} \tag{10}$$

with

$$\mathbf{M_{cc,app}}(\omega) = \mathbf{M_{cc}} - \mathrm{i}\omega \mathbf{M_{cv}} (\mathrm{i}\omega \mathbf{M_{vv}} + \mathbf{R_{vv}})^{-1} \mathbf{M_{vc}} \tag{11}$$

From an electrical point of view, the wall decreases the apparent inductance of the system as the current frequency is increased. This is consistent with Faraday's equation.

Note that this study is meaningful only in the case of the in-vessel design, since the ex-vessel design would not be powered at frequencies exceeding the wall penetration time.

5.3.1. Filament geometry for independent coil powering

In the general case of independent coil powering, the vessel filament geometry is chosen as follows. Each coil of the SCS is matched with a number of geometrically equivalent loops in the wall, taken as an infinite cylinder here. These loops are defined so that wall loops of two neighbouring coils are at most juxtaposed (see figure 11). Since the current density in the wall tends to tighten along the projection of the SCS coils as the frequency is increased, the values at the limit $\omega = \infty$ will be unaffected by the number of wall filaments outside the coil projection.

Note that the central column, the top and the bottom of the vessel are not taken into account in this representation of the vessel. Since these elements are relatively far away from the coils, neglecting them is certainly not too damaging. The $n = 0$ combination case (section 5.3.4) shows that this assumption has no major consequences.

5.3.2. Filament geometry for $n = 0$ coil combination

The $n = 0$ combination of the in-vessel SCS is of particular interest for vertical control, especially if a special common power supply is used for it. In order to calculate the magnetic field produced in $n = 0$ configuration, it is easier to replace the rows of the SCS by circular toroidal loops and to also use circular toroidal filaments to describe the wall. Such an assumption allows to take into account the remaining parts of the vessel (bottom, top and central column). In this context, the general method developed in section 5.3 still holds, but the calculation is greatly simplified by the axisymmetric geometry.

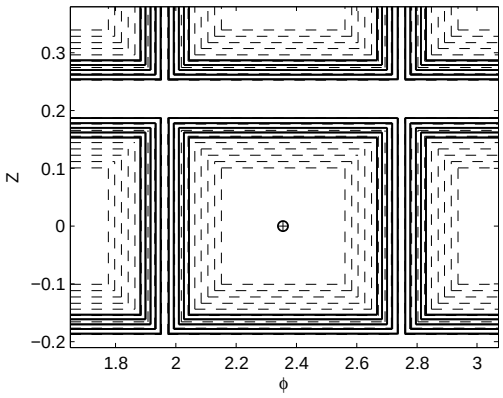

Figure 11: Illustration of the vessel filaments (in dashed lines) used in the case of independent coil powering. The number of filaments has been decreased here for the sake of clarity. The coil turns are represented by solid lines. The number of turns per coil in the figure is illustrative only.

The results obtained here are also useful to check the validity of the results obtained in the independent coil powering geometry. Note that this approach neglects the contribution from the vertical segments of the SCS and the toroidal gaps between the coils.

5.3.3. Apparent inductance as a function of frequency

The apparent self and mutual inductances as a function of frequency of the in-vessel system using the filament geometry for independent coil powering and equation (11) is shown in figure 12. Similarly to the DC case, coupling between coils at high frequency is weak and becomes negligible for coils that are not direct neighbours. For the sake of clarity, the apparent self-inductance of a single coil is shown separately in figure 13. The effect of the wall is not negligible, since the reduction of apparent inductance is close to a factor 2. Therefore, the required voltage to reach a given peak current at high frequency is smaller than what could be expected from DC values.

5.3.4. $n = 0$ coil combination and wall model consistency

When combining coils in $n = 0$ configurations, the total inductance of the system depends on the relative direction of the current between the coil rows. For simplicity, we assume that each coil row is either not active ('0') or carry the same current amplitude as the other rows ('+' or '-', depending on the

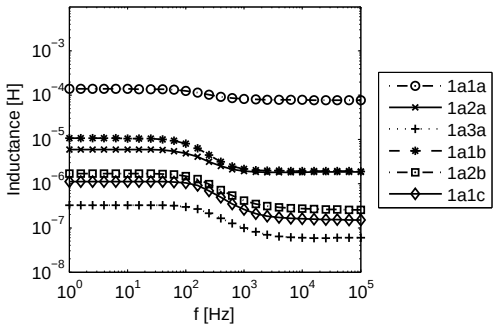

Figure 12: Apparent self and mutual inductances of a selection of pairs of coils as a function of frequency for the 10-turn in-vessel SCS, using the wall filament geometry described in section 5.3.1. A 2-character alphanumeric code is used to describe the coil locations, the digit indicating the location of a coil in a row and the letter indicating the coil row.

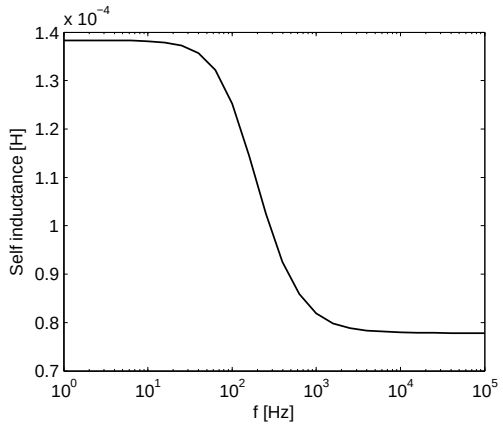

Figure 13: Apparent self inductance of a coil of the 10-turn in-vessel SCS as a function of frequency, using the wall filament geometry described in section 5.3.1.

current sign). In this case, the minimal inductance is obtained for the '0+0' configuration while the '+-+' configuration yields the largest inductance. The results for both type of wall filaments can be compared by grouping the apparent inductances obtained with the saddle-shaped wall filaments in $n = 0$

configurations (see figure 14). As expected, the DC inductance is slightly higher for the combination of saddle coils because of the contribution of the vertical segments of the coils. At high frequency, the decrease of apparent inductance due to the presence of the wall is slightly larger for the circular filament model, consistently with a better modelling of the screening effect due to a full spatial coverage of the vessel by the filaments. The discrepancy between both results is not significant from the engineering point of view and both approaches will be considered as satisfactory. Nonetheless, when possible, the worst situation results should be used for the power supply design, i.e. the inductance given by the saddle-shaped filament model and the effective vertical control given by the circular filament model.

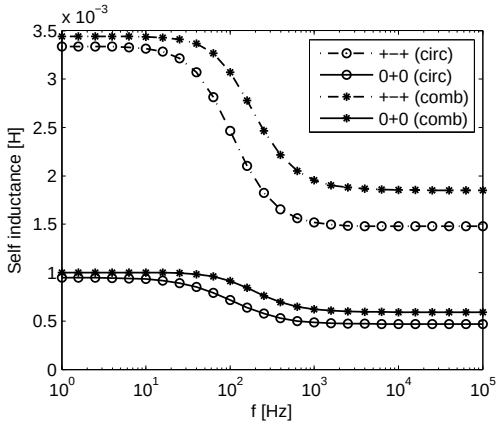

Figure 14: Apparent self-inductance of '0+0' and '+-+' $n = 0$ combinations of the 10-turn in-vessel SCS as a function of frequency. The results obtained for the toroidally circular wall filaments ("circ") are compared to the results obtained for the saddle-shaped filaments by combining the apparent inductances of the SCS coils obtained for that geometry ("comb").

5.3.5. Magnetic perturbation screening as a function of frequency

The 10-turn in-vessel SCS design is used to quantify the screening of the magnetic perturbation due to the vessel image currents. For that purpose, a single coil of the system is used so that the number of filaments in the wall can be increased both vertically and radially to obtain a more accurate description of the wall. Equation (6) is solved for a range of frequencies to obtain the wall currents. The radial magnetic field due to the coil and the

wall currents is averaged on the coil axis, limited by the radial extent of the vacuum chamber. This calculation is repeated for a selection of radial locations of the coil, going from 0 to 4 cm between the coil and the wall surfaces. The results are shown in figure 15. Note that the indicated distance to wall is measured from the coil center to the wall inner surface. On figure 15a, the saturation of the attenuation at high frequencies can be seen. The deviation of the attenuation along the radial coordinate is larger for the case where the coil is further away from the vessel wall, consistently with a larger spreading of the vessel currents and a non negligible distance between both sources of magnetic field with respect to the probed location. Figure 15b shows that the attenuation is strongly dependent on the distance from the coil to the wall. The coil centers of the original 10-turn design are located at 2.5 cm from the wall surface, in which case only approximately 25% of the perturbation remains at high frequency.

5.4. SCS reduced response function

Equation (10) defines the response functions of the SCS in the presence of a conducting wall. Note that the response functions of the different coils are coupled with one another and with the wall. Although each response function can be represented as a function of frequency in both directions ($I_c(U_c)$ and $U_c(I_c)$), they cannot be described by a simple analytical expression, as would be required to design the power supplies. In order to reduce the complexity of the system, the general method of system response reduction is used. This procedure is described below.

Equations (6) and (9) expressed in a more general form are written:

$$\mathbf{U} = \mathbf{M} \cdot \dot{\mathbf{I}} + \mathbf{R} \cdot \mathbf{I} \tag{12}$$

with

$$\mathbf{U} = \begin{bmatrix} \mathbf{U_c} \\ \mathbf{0} \end{bmatrix} \quad \mathbf{M} = \begin{bmatrix} \mathbf{M_{cc}} & \mathbf{M_{cv}} \\ \mathbf{M_{vc}} & \mathbf{M_{vv}} \end{bmatrix}$$

$$\mathbf{I} = \begin{bmatrix} \mathbf{I_c} \\ \mathbf{I_v} \end{bmatrix} \quad \mathbf{R} = \begin{bmatrix} \mathbf{R_{cc}} & \mathbf{0} \\ \mathbf{0} & \mathbf{R_{vv}} \end{bmatrix}$$

from which the time derivative of the currents is written:

$$\dot{\mathbf{I}} = -\mathbf{M}^{-1} \cdot \mathbf{R} \cdot \mathbf{I} + \mathbf{B} \cdot \mathbf{U_c} \tag{13}$$

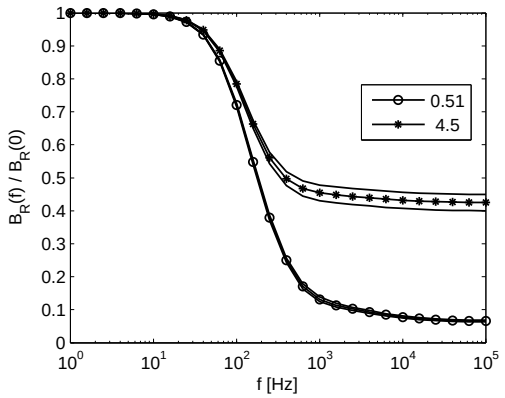

(a) Scan on frequency

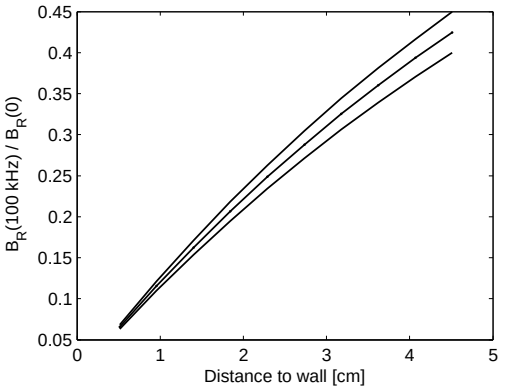

(b) Scan on distance to the wall

Figure 15: Mean attenuation along the coil axis of the magnetic perturbation created by the 10-turn in-vessel SCS. (a) frequency dependence for two different distances from the coil center to the wall surface (in centimeters), including the standard deviation along the radial coordinate. (b) dependence on the distance to the wall at saturation (i.e. 100 kHz), also including the standard deviation.

with $\mathbf{B}$ the first n_c columns of $\mathbf{M}^{-1}$. In this form, the circuit equation is an example of a linear time invariant system (**LTI**) and the tools developed in the frame of LTI theory are applicable.

LTI theory involves the manipulation of state-space models. A general state-space model formulation is given by:

$$\begin{cases} \dot{\mathbf{x}} = \mathbf{A}\mathbf{x} + \mathbf{B}\mathbf{u} \\ \mathbf{y} = \mathbf{C}\mathbf{x} + \mathbf{D}\mathbf{u} \end{cases} \tag{14}$$

where $\mathbf{u}$ is the input, $\mathbf{y}$ the output and $\mathbf{x}$ the space vector of the system. Of course, $\mathbf{u}$ and $\mathbf{y}$ can also be vectors, in which case the system is said to be a MIMO (multiple inputs, multiple outputs). Writing $\dot{\mathbf{x}} = s\mathbf{x}$, the transfer function $\mathbf{G}(s) := \mathbf{y}/\mathbf{u}$ is given by:

$$\mathbf{G}(s) = \mathbf{C}(s\mathbb{1} - \mathbf{A})^{-1}\mathbf{B} + \mathbf{D} \tag{15}$$

Note that $\mathbf{G}$ is a matrix of transfer functions in the general case.

In the case of the wall filament model, the state space model is given by comparing equations (13) and (14): $\mathbf{x} := \mathbf{I}$, $\mathbf{A} := -\mathbf{M}^{-1} \cdot \mathbf{R}$, $\mathbf{B} := \mathbf{B}$, $\mathbf{u} := \mathbf{U_c}$, $\mathbf{y} := \mathbf{I_c}$, $\mathbf{C} = [\mathbb{1}_\mathbf{c}, \mathbf{0}]$ and $\mathbf{D} = \mathbf{0}$. In equation (14), $\mathbf{x}$ is an internal variable. It is therefore possible to approximate the transfer functions corresponding to the state-space model by reducing the dimensions of the space vector and the state matrix $\mathbf{A}$. In terms of response function, such an approach is equivalent to cancelling close pole-zero pairs. In the formalism of LTI systems, a Hankel singular value decomposition (HSVD) is used to obtain such a system reduction. The wall filament model leads to a problem of degeneracy, each coil and its set of wall filaments being identical or very close to one another. To obtain a correct reduction of the order of the system, the degeneracy must be alleviated beforehand by replacing the multiple input by a single one, so that the system becomes asymmetric. The system order reduction by HSVD is then determined by the desired reduced system order and the conservation of the DC gain of the system. Generally, the reduced system order should be as low as possible and the DC gain should be conserved while keeping a good approximation of the original system. These aspects are studied in the analysis given below. Note that the state-space description of a LTI system is exactly equivalent to a zero-pole-gain description. Therefore, a reduced system can be converted to a set of transfer functions with a number of poles and zeros given by the order of the reduced system.

The numerical analysis is performed on the 10-turn in-vessel SCS. Due to the symmetry of the SCS and to the weak coupling between coils, it is sufficient to consider one of the middle row coils as input of the system. Two questions are then addressed: what is the adequate reduced system order and should the equivalent DC gain constraint be used? The study concerning the model reduction is presented in figure 16. An order of 3 has been chosen to reduce the model since, as shown, the response function is well approximated in the range of frequencies of experimental interest. A lower order would result in a sufficient approximation quality only on a reduced frequency interval, while a higher order would lead to unnecessary complication of the analytical expression of the transfer functions. In general, system reduction by truncation results in a much better approximation of the transfer functions, at the cost of a small discrepancy on the DC gain. In our case, this discrepancy is negligible and the truncation method should be kept.

6. Vertical control

In the current TCV setup, vertical control (**VC**) is successfully provided by the internal fast coils, also called *G*-coils. Since the co-existence of two internal coil systems is problematic in terms of space occupation, not only with the coils themselves but also with feedthroughs and power lines, the questions of replacement of the actual *G*-coils by the in-vessel SCS and the conditions under which this replacement can occur must be addressed. In this section, the applicability of the in-vessel SCS to vertical control is studied, using a principle of equivalence with the present system, a 3-turn coil whose turns are located in both LFS corners of the vacuum vessel (see figure 2) and fed with a maximum of 2 kA.

6.1. Vertical control principle

Vertical control is obtained by applying a magnetic field with a dominant component along the main radial coordinate. Combined with the plasma current, this field gives rise to a vertical Laplace force whose direction and amplitude are adjusted to counteract a vertical displacement of the plasma. Since these corrections must be applied on short time scales, the vessel wall screening currents must be taken into account when dimensioning the amplitude of the control radial field.

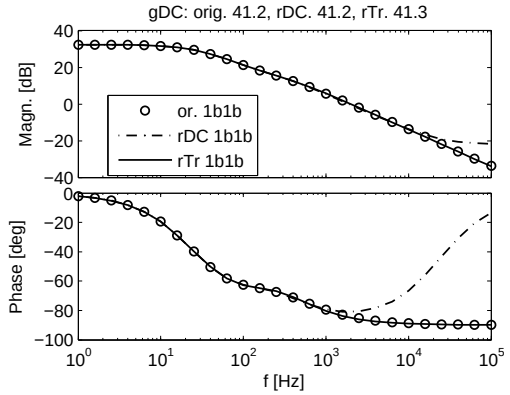

(a) Self

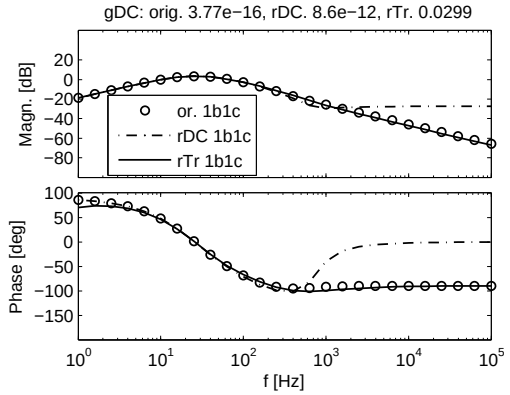

(b) 1 row apart

Figure 16: Original and reduced (order 3) response functions between different pairs of coils of the 10-turn in-vessel SCS. Original model: 'or'. Reduced model with DC gain constraint: 'rDC'. Reduced model by simple truncation of small singular values: 'rTr'. The DC gains for each case are given in the figure titles. Each considered coil is labelled by a two-character alphanumeric symbol, the digit representing the toroidal position and the letter indicating the coil row.

6.2. Calculation method

As vertical control is obtained by $n = 0$ combinations of the coils, the circular toroidal filament model (section 5.3.2) is used to represent the vessel wall. Equation (6) is used to get the wall currents as a function of frequency for a given coil combination. The effective radial control field at each point of the Tokamak poloidal cross-section is obtained by adding up the contribution of the coil system with the contribution of the vessel wall. Note that only the high frequency results are of interest for this analysis.

Since three independent coil rows are available, different row combinations are possible. Using the same labelling as in section 5.3.4, the possible non redundant combinations creating the highest possible radial field are: '+++', '-++', '++-' and '+-+'.

In order to assess the efficiency of the different coil row combinations and to compare them with the control capacity offered by the G-coils, a series of synthetic plasma current distributions is generated to cover a range of typical situations occurring in TCV. The series of synthetic current distributions is expressed as follows:

$$\begin{cases} j_{aux}(R,Z) = 1 - \left(\frac{R-R_0}{a}\right)^2 - \left(\frac{Z-Z_0}{b}\right)^2 & \\ j(R,Z) = j_{mag} j_{aux}(R,Z) & j_{aux} \geq 0 \\ j(R,Z) = 0 & j_{aux} < 0 \end{cases} \tag{16}$$

with

$$\begin{array}{lcl} R_0 & = & 0.872\,m \\ Z_0 & = & 0 \quad \text{or} \quad 0.23\,m \\ a & = & 0.225\,m \\ b & = & 2a \quad \text{or} \quad 3a \\ j_{mag} & = & 10^6 \frac{b}{3a} \frac{1}{\int j_{aux} \mathrm{d}R\mathrm{d}Z} \end{array} \tag{17}$$

In other words, an elliptic cross-section with quadratic current profile is used. $R_0 = 0.872$ corresponds to the vessel center, accounting for the new position of the tiles due to the saddle coil system. $b = 3a$ corresponds to an elongated plasma and is used only when $Z_0 = 0$. The current density is scaled to give a total plasma current of 1 MA at the largest elongation.

For each current distribution, the vertical component of the Laplace force is calculated and integrated over the plasma poloidal cross-section. The force per unit current serves as a comparison parameter between the different coil row combinations, while the current required to provide a force equal to the force provided by the G-coils gives the equivalent current I_{equiv} for each case.

6.3. Optimal coil row combinations

The vertical forces created by the SCS in optimal coil row combinations for given plasma current distributions, defined as the combinations delivering the largest vertical force per unit current at high frequency, are plotted as a function of frequency in figure 17. In general, the best row combination at high frequency is also the best combination at low frequency. For the elongated plasmas, this is however not the case (see figure 17b). This is due to an increased importance of the coil segments located in the corners of the vessel for highly elongated plasmas. At low frequency, these segments have a strong contribution to the vertical force, resulting in an optimal combination of type '+++', while at high frequency these segments are more efficiently screened by the vessel than the other coil segments and have a weaker contribution, therefore leading to an optimum given by the '+-+' combination. In figure 17b, the results for all the up-down symmetric combinations in the case of a highly elongated plasma located at $z_{mag} = 0$ are plotted. Since the vertical force obtained for the '+-+' combination dominates above 50 Hz, it can be safely considered as the optimal combination for this kind of plasmas. If lower frequencies are of importance, the '0+0' combination could be a possible consensus between efficiencies at low and high frequencies.

6.4. Current requirements

The vertical force provided by the G-coil for the three plasma current distributions is compared to the force provided by the in-vessel SCS in figure 18a. The force ratio displayed in the figure is defined as:

$$r_F = [F_{Z,G}/(I_G N_G)] \,/\, [F_{Z,SCS}/(I_{SCS} N_{SCS})] \tag{18}$$

where I is the current in the respective coils and N the number of turns. The required current for the SCS is obtained by: $I_{SCS,equiv} = 6 \cdot 10^3 \cdot r_F$ [At]. The most demanding situation, i.e. highly elongated plasmas, corresponds to a required current of 4.05 kAt. This value might change if the SCS geometry is modified and should therefore be considered as indicative. Based on a 20% safety margin, a current of 5 kAt must be considered for vertical control. Note that this value is inferior to the 6 kAt of the G-coil system. The SCS provides a much better control for low elongation plasmas located at $z_{mag} = 0$ (factor 5 at high frequencies), but these plasmas are less vertically unstable than the highly elongated ones.

For the sake of completeness, the results for different sensible coil combinations in the high elongation case are shown in figure 18b. Keeping in

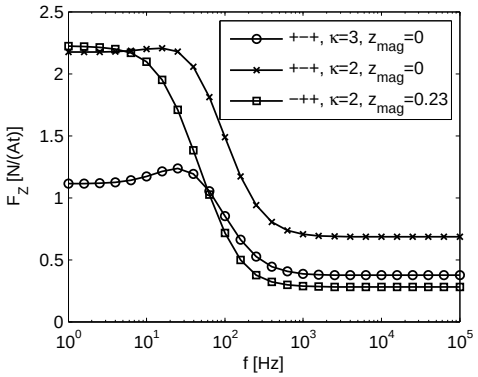

(a) Optimal combinations

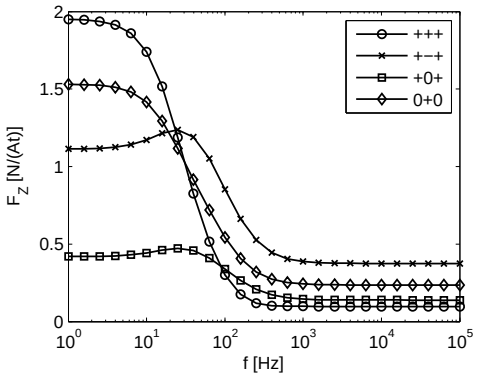

(b) Highly elongated plasma

Figure 17: Vertical force exerted by the 10-turn in-vessel SCS. (a) optimal $n = 0$ combinations for a selection of plasma current distributions. (b) different $n = 0$ combinations for a highly elongated plasma located at $z_{mag} = 0$.

mind that the optimal combination is determined by the smallest force ratio, the frequency response of the vertical force provided by the G-coil does not change the conclusions given previously for the choice of optimal row combination. For high elongation plasmas, the G-coil is better than all the possible combinations at low frequency because it creates a magnetic field that has a radial component of constant sign across the whole plasma.

7. Effects of disruptions

Plasma disruptions induce large currents in the Tokamak vessel and in any internal coils. It is therefore necessary to estimate the maximal voltage and current that coils of the SCS will endure during disruptions. This study is presented in this section.

7.1. Disruption models

Two kind of disruptions are considered in this study: vertical disruptions and plasma current quenching. Vertical disruptions are modelled by a 20 cm vertical shift of the plasma on a characteristic time of 250 μs. Current quenching disruptions are modelled by a linear decrease of the plasma current from its initial value to zero on a typical time of 1 ms. The different values given here are typical of TCV disruptions. The initial plasma states are described in terms of current density distributions, as defined in section 6.2. For this study, the number of conditions is nonetheless increased: Z_0 is scanned from 0 to 0.5 m by step of 0.1 m and $b = 3a - |Z_0|$. The plasma is represented by toroidal circular current filaments. The vessel wall is modelled by the circular toroidal filament model (section 5.3.2), but the real geometry of the SCS coils is used. With this choice, the wall and coil models are not consistent, but the small error due to this inconsistency (recall that the perturbation is in $n = 0$) is negligible compared to the benefit of using the correct self-inductance of the coils. For simplicity, the time traces of the plasma filament currents $I_x(t)$ are chosen to be linear by parts. For vertical disruptions of shift $\Delta Z = \pm 0.2$ m, the current variation in the plasma filament is given by $\Delta I_x(Z) = I_{x,0}(Z - \Delta Z) - I_{x,0}(Z)$ where $I_{x,0} = I_x(t = 0)$. For current quenching disruptions, ΔI_x is simply given by $\Delta I_x = -I_{x,0}$. The current variation occurs linearly during a time τ.

In order to find the voltages and currents in the SCS, the coupled voltage equations of the SCS and the vessel wall must be solved for all times, using

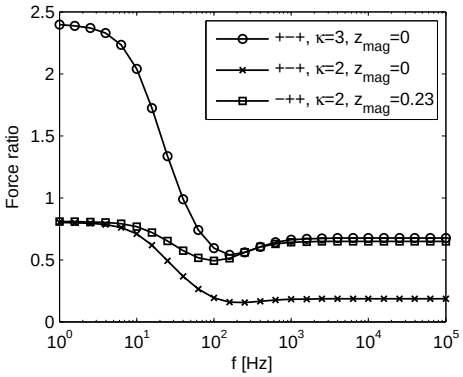

(a) Optimal combinations

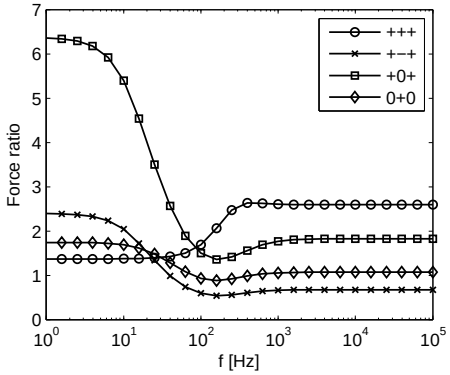

(b) High elongation plasmas

Figure 18: Ratio of the vertical forces per unit current per turn of the G-coil and the 10-turn in-vessel SCS in optimal combinations for all the plasma current distributions (a) and in all sensible combinations for the high elongation case (b).

the plasma current variation as a source term. These equations are written:

$$\mathbf{R_{ss}I_s} + \mathbf{M_{ss}}\partial_t\mathbf{I_s} + \mathbf{M_{sx}}\partial_t\mathbf{I_x} = \mathbf{0} \tag{19}$$

with

$$\mathbf{R_{ss}} = \begin{bmatrix} \mathbf{R_v} & \mathbf{0} \\ \mathbf{0} & \mathbf{R_c} \end{bmatrix},\ \mathbf{I_s} = \begin{bmatrix} \mathbf{I_v} \\ \mathbf{I_c} \end{bmatrix},$$

$$\mathbf{M_{ss}} = \begin{bmatrix} \mathbf{M_{vv}} & \mathbf{M_{vc}} \\ \mathbf{M_{cv}} & \mathbf{M_{cc}} \end{bmatrix},\ \mathbf{M_{sx}} = \begin{bmatrix} \mathbf{M_{vx}} \\ \mathbf{M_{cx}} \end{bmatrix}$$

with c the SCS coil index, v the vessel filament index, $s = c + v$, x the plasma filament index, $\mathbf{M_{ab}}$ the mutual inductance matrix between systems a and b, $\mathbf{R_a}$ the diagonal matrix of resistances of system a and $\mathbf{I_a}$ the current in system a. The resolution of equation (19) is described in Appendix B. Knowing $\mathbf{I_c}$, the voltage induced by the plasma disruption in the SCS is given by:

$$\mathbf{U_c} = \mathbf{R_{cc}I_c} + \mathbf{M_{cc}}\partial_t\mathbf{I_c} \tag{20}$$

7.2. Induced voltage and current

The maximal voltage and current induced by a plasma disruption in the 10-turn in-vessel SCS is obtained by calculating $\mathbf{I_c}(t)$ (19) and $\mathbf{U_c}(t)$ (20) for each initial plasma current distribution and keeping the maximal value over time, distributions and SCS coils. The results for a scan on τ are shown in figure 19. For the studied interval of values of τ, the induced current remains approximately constant and the largest value is obtained for a disruption of type plasma current quenching. The voltage is larger for the same type of disruption, but since the characteristic time is smaller for vertical disruptions, their related voltage is higher. The worst situations therefore results in 16.5 kAt of induced current and 51 V/t of induced voltage. Note that only the resistance and the inductance of the SCS coils have been taken into account in the calculation. A more realistic description should also consider the feeding line inductance and resistance, as well as the presence of safety resistances along the current path. In that case, the voltage would remain the same, but the induced current would be decreased.

8. Magnetic forces on the SCS

This section describes the aspect of magnetic forces endured by the in-vessel SCS in a worst-case scenario, i.e. the situation leading to the highest force amplitude.

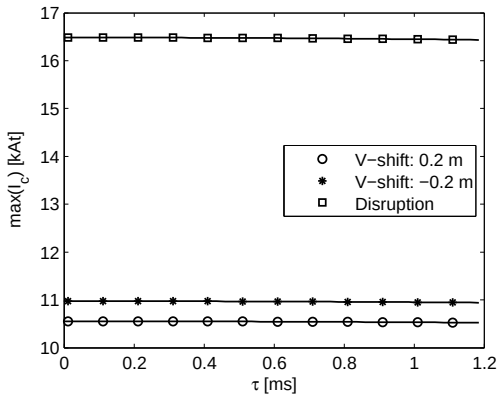

(a) Induced current

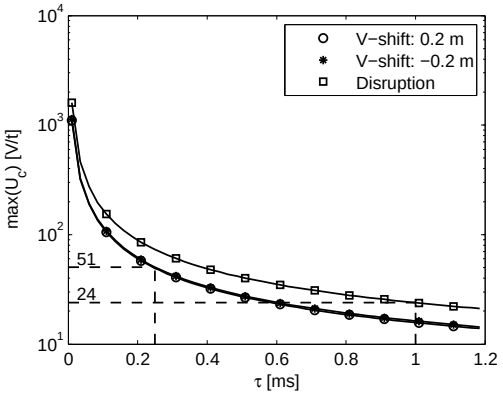

(b) Induced voltage

Figure 19: Maximal current and voltage induced in the coils of the 10-turn in-vessel SCS for three types of plasma disruptions with characteristic time τ. The maxima are taken over a series of plasma current distributions, time evolution and SCS coils.

8.1. Origin of the magnetic forces

Magnetic forces are exerted on the coils when the magnetic field at the coil location has a non zero component perpendicular to the coil segments. They are described by the Laplace force formula:

$$\mathbf{F}_N(s) = I_N \mathbf{e}_s \times \mathbf{B}(s)\,[\mathrm{N/m}] \tag{21}$$

where s is a linear coordinate along the coil turns, $\mathbf{F}_N(s)$ is the Laplace force density per turn at s, I_N is the current flowing in the coil, $\mathbf{e}_s$ is the unit vector along the coil turn and $\mathbf{B}(s)$ is the total magnetic field at s.

The current I_N flowing in the coil is given by the sum of the desired applications of the SCS and the current induced by a disruption. In the worst-case scenario, all these currents are present simultaneously, so that:

$$I_N = I_{N,nominal} + I_{N,disr} = \frac{I_{RMP} + I_{EFC} + I_{VC}}{N} + \frac{I_{disr}}{N} \tag{22}$$

with $I_{RMP} = 4\,\mathrm{kAt}$, $I_{EFC} = 3\,\mathrm{kAt}$, $I_{VC} = 5\,\mathrm{kAt}$, $I_{disr,top} = 16.5\,\mathrm{kAt}$ and $I_{disr,mid} = 12.1\,\mathrm{kAt}$ for the $N = 10$-turn in-vessel SCS (coil in short-circuit). Note that the difference between the disruption-induced currents in each coil row is retained in this section.

The magnetic field at the coil location is the sum of the contributions from the poloidal coils $\mathbf{B_a}$, the toroidal coil $\mathbf{B_T}$, the plasma current $\mathbf{B_p}$, the vessel currents at disruption $\mathbf{B_v}$ and the saddle coils (neighbours and coil themselves) $\mathbf{B_c}$. For each source, the worst-case scenario must be considered: the coils must be powered at their maximal current, a series of plasma current distributions must be considered and the disruptions inducing the strongest currents must be used in the calculation.

8.2. Maximal magnetic field and force calculation

The magnetic field related to the different sources is calculated on each point of the SCS. Points are considered independently and the worst situation is kept for each point and each source. The magnetic fields are combined in absolute value whenever a possible constructive superposition of the fields is encountered.

The magnetic field due to the poloidal coils is given by:

$$\mathbf{B_a}(s) = |\mathbf{G^R_{sa}}|\mathbf{I_{nom,a}}\mathbf{e_R} + |\mathbf{G^Z_{sa}}|\mathbf{I_{nom,a}}\mathbf{e_Z} \tag{23}$$

with $\mathbf{I_{nom,a}}$ the maximal currents in the poloidal coils, $\mathbf{G^R_{sa}}$ and $\mathbf{G^Z_{sa}}$ the (R, Z) components of the magnetic field at s due to a unit current in coil a. The G-coils are not included here since the SCS should replace them.

The magnetic field due to the toroidal coil is given by:

$$\mathbf{B_T}(s) = |G^R_{sT} I_{nom,T}|\mathbf{e_R} + |G^\phi_{sT} I_{nom,T}|\mathbf{e}_\phi \tag{24}$$

with $I_{nom,T}$ the maximal current in the toroidal coil, G^R_{sT} and G^ϕ_{sT} the (R, ϕ) components of the magnetic field at s due to a unit current in the toroidal coil.

The series of representative plasma current distributions used in the study of disruption effects (section 7.1) is used to calculate the magnetic field due to the plasma current:

$$\mathbf{B_p}(s) = \max_{Z_0}(|\mathbf{G^R_{sx}} \cdot \mathbf{I_x}(Z_0)|)\mathbf{e_R} + \max_{Z_0}(|\mathbf{G^Z_{sx}} \cdot \mathbf{I_x}(Z_0)|)\mathbf{e_Z} \tag{25}$$

with $\mathbf{I_x}(Z_0)$ the currents in the plasma filaments x for the current distribution labelled by Z_0, $\mathbf{G^R_{sx}}$ and $\mathbf{G^Z_{sx}}$ the (R, Z) components of the magnetic field at s due to a unit current in filament x.

The worst-case magnetic field due to the currents induced in the Tokamak vessel during a plasma disruption is calculated with:

$$\mathbf{B_v}(s) = \max_{\text{disr. case}}(|\mathbf{G^R_{sv}} \cdot \mathbf{I_v}(\text{disr. case})|)\mathbf{e_R} + \max_{\text{disr. case}}(|\mathbf{G^Z_{sv}} \cdot \mathbf{I_v}(\text{disr. case})|)\mathbf{e_Z} \tag{26}$$

with $\mathbf{I_v}(\text{disr. case})$ the matrix of vessel filament currents, each column corresponding to one of the studied disruption cases (see section 7.1), $\mathbf{G^R_{sv}}$ and $\mathbf{G^Z_{sv}}$ the (R, Z) components of the magnetic field at s due to a unit current in filament v.

The magnetic field due to the saddle coils themselves is also considered in this analysis. The sources are reduced to the direct neighbouring coils (top t, bottom b, left l, right r) and the coil itself i. Due to the symmetry of the system, only two target coils need to be considered: one coil of the middle row and one coil of the top row. The worst case magnetic field per unit current is then given by:

$$\mathbf{G_{c,top}}(s) = \sum_{k \in \{i,l,r,b\}} (1 + c_{\text{top},k}) \sum_{x \in \{R,Z,\phi\}} |\mathbf{G^x_{sk}}|\mathbf{e_x} \tag{27}$$

$$\mathbf{G_{c,\mathrm{mid}}}(s) = \sum_{k\in\{i,l,r,t,b\}} (1 + c_{\mathrm{mid},k}) \sum_{x\in\{R,Z,\phi\}} |\mathbf{G^x_{sk}}|\mathbf{e_x} \tag{28}$$

with $\mathbf{G^x_{sk}}$ the x-component of the magnetic field at s due to a unit current in coil k ($k \in \{t, b, l, r, i\}$), $c_{\mathrm{top},k} = \delta_{kb}(\frac{I_{N,\mathrm{mid}}}{I_{N,\mathrm{top}}} - 1)$, $c_{\mathrm{mid},k} = (\delta_{kt} + \delta_{kb})(\frac{I_{N,\mathrm{top}}}{I_{N,\mathrm{mid}}} - 1)$ and δ_{kj} the Kronecker symbol. $c_{\mathrm{top},k}$ and $c_{\mathrm{mid},k}$ are correction factors to obtain the correct forces when multiplying by $I^2_{N,\mathrm{top}}$ and $I^2_{N,\mathrm{mid}}$ respectively.

The worst-case force density per turn is then given by:

$$\mathbf{F_{turn}}(s) = I_N \mathbf{e_s} \times [\mathbf{B_a} + \mathbf{B_p} + \mathbf{B_v} + \mathbf{B_T}] + I^2_N \mathbf{e_s} \times \mathbf{G_c}\,[\mathrm{N/m}] \tag{29}$$

The total force density on the coil is obtained by adding up the forces on each turn. In the process, the variation of the sign of $\mathbf{G_{si}}$ (the field created by a saddle coil on itself) on the coil cross-section can be explicitly accounted for:

$$\begin{aligned}\mathbf{F_{coil}}(\mathbf{s}) = &\\ &\sum_{\mathrm{turns}} \Big|\big[I_N \mathbf{e_s} \times [\mathbf{B_a} + \mathbf{B_p} + \mathbf{B_v} + \mathbf{B_T}] + I^2_N \mathbf{e_s} \times (\mathbf{G_c} - |\mathbf{G_{si}}|)\big]\Big| \\ &+ \left|\sum_{\mathrm{turns}} I^2_N \mathbf{e_s} \times \mathbf{G_{si}}\right| [\mathrm{N/m}]\end{aligned} \tag{30}$$

Note that the force calculated in (30) is expressed as a linear density. Its value corresponds to the maximal force that could be exerted independently on each point of the coil, with no information on the sign of this value. Consequently, a direct interpretation in terms of torque would be incorrect. Also note that each value corresponds to a maximum over a number of combined situations which have little chance of happening simultaneously in reality. For the sake of simplicity, the coil current I_N and the worst-case magnetic field are calculated independently. The worst-case magnetic fields due to the vessel currents and the plasma current are also calculated independently.

8.3. Results and discussion

The calculation of the worst-case magnetic field at the SCS location using equations (23), (24), (25), (26), (27) and (28) leads to the following conclusions. For the R-component, the most important contribution comes from the poloidal coils, the toroidal coil contribution is negligible, the plasma and vessel contributions are in the same range, representing approximately a fifth of

the poloidal coil contribution, and the SCS contribution is important on the edge turns of the winding. For the Z-component, similar observations can be made for the poloidal coil contribution with respect to the plasma and vessel contributions. The SCS contribution is nonetheless much smaller. Finally, the ϕ-component contribution of the SCS is comparable to its Z-component contribution and is much smaller than the toroidal coil contribution.

When considering the spatial variation of the magnetic field across a coil of the SCS, a scan on the different combinations of sources of magnetic field shows that it can display variations of amplitude across a coil equal to its maximal amplitude, therefore leading to important gradient of magnetic forces.

The total worst-case force density on each coil, as calculated with (30) is shown in figure 20. A maximal force density of 50 kN/m is to be expected when considering all the possible sources of magnetic field together. The contribution of the SCS itself is of 20% at most, since it mainly appears as a force oriented towards the coil winding center that cancels out when adding up the coil turns.

9. Number of turns per coil

Although the number of turns per coil is not a relevant issue from the point of view of the physical applications of the SCS, it is an important aspect when discussing engineering constraints. This section gathers a number of arguments related to the number of turns per coil and details how the main electrical parameters scale with it.

9.1. Mechanical aspects

For a small number of turns (1 to 3), a rigid material (e.g. GlidCop) can be chosen so that each turn is self-supporting. In that case, the insulating material would be limited to coil supports. For a large number of turns (more than 3), the turns must be packed together to ensure rigidity. In that case, each turn must be coated with an insulating material. This material must be able to withstand the thermal expansion due to vessel baking and Joule effect and be vacuum compatible. In the case of a large number of turns per coil, a smaller cross-section is allowed for the connection lines from the feedthroughs to the coils. In addition, smaller magnetic forces would be exerted on these conductors, so that their mounting point could be less resistant mechanically.

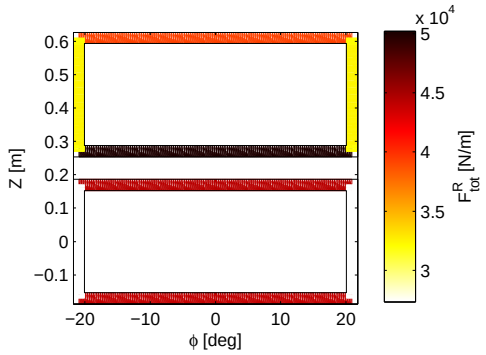

(a) F^R_{coil}

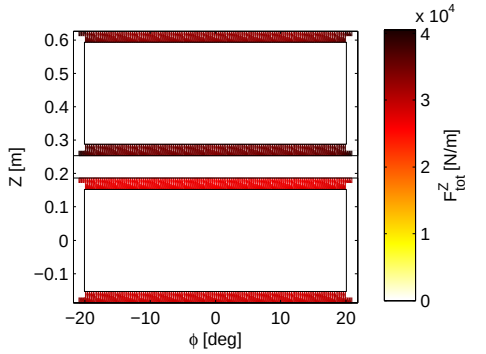

(b) F^Z_{coil}

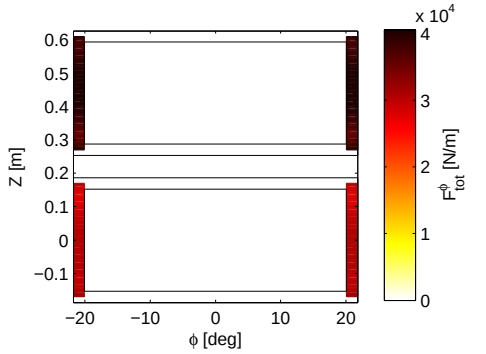

(c) F^ϕ_{coil}

Figure 20: Absolute value of the total force density on the coils in each direction.

9.2. Electrical aspects

Note: In the following, the index N corresponds to a N-turn coil while the index 1 corresponds to an equivalent single-turn coil.

Required current : The electrical specifications of the coils of the SCS are given in terms of effective required current: $I_{req,1} = NI_{req,N}$. $I_{req,1}$ itself is made of a near DC component for RMP and EFC ($I_{req,DC} = I_{RMP} + I_{EFC}$) and a high frequency component for vertical control ($I_{req,hf} = I_{VC}$).

Cross-section : The effective conductor cross-section is determined by the allowed increase of temperature during a duty cycle of the SCS due to Joule effect. The current value used for this calculation might depend on the exact physical application, but in general $I_{req,DC}$ should be used. The adiabatic variation of temperature ΔT of a conductor due to Joule effect is given by:

$$\Delta T = \frac{\rho_{el}}{\rho_m c} \frac{\int I^2 \mathrm{d}t}{S^2} \tag{31}$$

where ρ_{el} is the electric resistivity, ρ_m the mass density, c the heat capacity, I the current and S the cross-section. In order to maintain a constant temperature variation of the different possible coil designs, the current density must remain constant: $S_N = S_1/N$. S_1 must be chosen to obtain a tolerable ΔT. Note that even though the overall conducting cross-section remains constant with N, the coil cross-section increases with N due to the thickness of the insulator between the turns.

Skin effect : For small values of N, the skin effect might become a problem at high frequency, leading to a non uniform distribution of temperature on the conductor cross-section. The skin depth δ at frequency f is given by $\delta = \sqrt{(2\rho_{el})/(2\pi f \mu_0 \mu_r)}$ where μ_r is the relative permeability of the conductor. Writing f_{skin} the effective fraction of conducting surface and considering an AC current, equation (31) becomes:

$$\Delta T = \frac{\rho_{el}}{\rho_m c} \frac{\int I_{peak}^2 \mathrm{d}t}{2 f_{skin}^2 S^2} \tag{32}$$

The contribution of the skin effect, appearing through $1/f_{skin}^2$, might therefore be important. It must however be noted that the temperature variation of the whole conductor, after diffusion from the edge to the

core, only goes as $1/f_{skin}$. In addition, the integral of the AC current results in the presence of a factor 1/2 which lessens the importance of the skin effect. Finally, since most of the temperature increase is related to $I_{req,DC}$, this high frequency issue should usually not be important. In advanced applications, like RWM or rotation control, it might however be relevant. Note that the *proximity effect* related to the juxtaposition of coil turns in AC mode has not been accounted for here.

Resistance : The resistance of a N-turn coil is given by $R_N = N^2 R_1$.

Inductance : The mutual inductance between the turns of a coil is at most equal to the self-inductance of each turn. Therefore: $L_N \simeq N^2 L_1$. At high frequency, the apparent inductance can be approximated by $L_N(\omega \to \inf) \simeq N^2(L_1 - C_1)$ where C_1 is the coupling term of a single-turn coil with an ideal wall (see equation (11)).

Voltage : The power supply voltage U is determined by the time required to reach a given current in the coils. The step response of RL-circuits can be approximated by $I(t) \simeq (U/L)t$ as long as t is small compared to the characteristic time $\tau_{RL} = L/R$. The error between the approximation and the exact solution is smaller than 10% if $t \leq 0.19\tau_{RL}$, i.e. in the first 20% of the current ramp. For a N-turn coil, it gives:

$$U_N = \frac{1}{\tau_{req}} I_{VC,N} L_N(\omega) \simeq N \frac{1}{\tau_{req}} I_{VC,1} \left(L_1 - \alpha(\omega) C_1\right) \qquad (33)$$

with τ_{req} the time required to reach $I_{VC,1}$ and $\alpha(\omega)$ the proportion of wall coupling. If τ_{req} is small enough, $\alpha = 1$. In addition, $\tau_{req} \leq 0.19\tau_{RL}$ and $U \geq N R_1 (I_{RMP,1} + I_{EFC,1} + I_{VC,1})$ must be satisfied.

Magnetic forces : During normal operation, the total force on a coil of the SCS is given by the sum of the forces on each turn of the coil and is therefore independent of N. In case of disruption, the induced voltage is proportional to N and the induced current is consequently going as $1/N$. The total force on the coil is hence independent of N in that case as well.

The different parameters described above are calculated here in the case of the 10-turn in-vessel SCS. In order to assess the robustness of the scaling with N, the results are also given for a single-turn SCS equivalent to the

10-turn system in terms of dimensions, cross-section and location. For both cases, the coils are assumed to be made of GlidCop (see table 3). Calculation results for $\tau_{req} = 250\mu$s are given in table 2. The disruption induced voltage and current have been added to the list of parameters, as well as the maximal magnetic force density exerted on the coil. The cross-section is slightly different between both cases because of the room left for the insulator in the 10-turn case. The most noticeable deviation from the scalings given above occurs for the self-inductance calculation. A multi-turn coil has a lower self-inductance than what would be predicted by the N^2 scaling because the spatial spreading of the turns with respect to one another results in a mutual inductance smaller than the self of each turn. The voltages obtained for each case satisfy the conditions stated above: $0.19\tau_{RL}$ is well above τ_{req} and U is sufficient to reach the total DC current. Note that the inductance and resistance of the power lines have not been accounted for in the given results.

Parameter	1-turn	10-turns
I_{RMP} [kA]	4	0.4
I_{EFC} [kA]	3	0.3
I_{VC} [kA]	5	0.5
S_N [mm^2]	300	28.9
ΔT (2s I_{DC}) [K]	9.6	10.3
R [Ω]	$2.4 \cdot 10^{-4}$	$2.4 \cdot 10^{-2}$
L_{DC} [μH]	1.58	138
L_{sat} [μH]	0.96	77.8
$\tau_{RL,DC}$ [ms]	6.5	5.7
$\tau_{RL,sat}$ [ms]	4.0	3.2
$U(\alpha = 0)$ [V]	32	277
$U(\alpha = 1)$ [V]	19	156
I_{disr} [kA]	16.9	1.65
U_{disr} [V]	58	510
$F_{coil,max}$ [kN/m]	51	50

Table 2: Various parameters of the 10-turn in-vessel SCS system and its single-turn equivalent. The symbols and the mathematical approaches are described in sections 7, 8 and 9.2.

Given the required raise time of 250 μs, the maximal frequency in AC mode is of 1 kHz. Using GlidCop parameters and a relative magnetic per-

meability of 1 (copper and aluminium values), the skin depth at 1 kHz is 2.7 mm. For $N \geq 10$, the increase of resistance due to skin effect should be negligible, especially if the conductor cross-section aspect ratio is large. Nonetheless, the proximity effect should be assessed on the final coil design. For a smaller number of turns, the skin effect will be important. Note that the resistance can increase by a factor 4 before an adaptation of the required voltage is needed.

10. Coil cooling

Due to Joule effect, the coils of the SCS will heat up during operation. This section addresses the issue of coil heating and cooling in a generic approach. Its aim is to quantify the main thermal parameters in order to identify relevant engineering issues and deduce physical arguments to orient the coil design. A detailed calculation of heat transport, if relevant, should be done once the final coil design is known.

10.1. Lamellar structure model

In this study, coils are modelled by a linear lamellar structure as described in figure 21. As shown, the coil folding is ignored (each turn has the same length even though the turns remain conceptually connected in series), turns are piled only in the z direction and each type of material has layers of constant thickness. The y direction corresponds to parallel heat transport while the z direction corresponds to perpendicular heat transport.

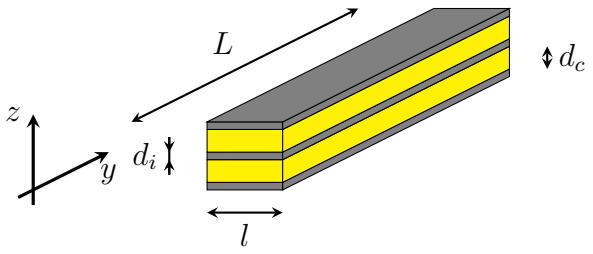

Figure 21: Coil model for heat transport calculation. L is the length of the coil, l its width, d_i the thickness of an insulator layer, d_c the thickness of a conductor layer, the z axis defines the perpendicular conduction direction and the y axis the parallel one.

10.2. Thermal properties of lamellar structures

When dealing with composite structures, as the lamellar model used here, it is convenient to reduce the physical constants of the different components to average values valid for the whole structure. This operation is detailed here for the specific heat capacity and the thermal conductivity. Considering a structure made of N_j layers of thickness d_j of material j (here $j \in \{i, c\}$), the total thickness of material j is $D_j = N_j d_j$, its fraction $f_j = D_j/D$ and the overall total thickness $D = \sum D_j$. Writing $\rho_{m,j}$ the mass density of material j and c_j its specific heat capacity, its volumetric heat capacity is given by $C_j = \rho_{m,j} c_j$. The average volumetric heat capacity is then given by:

$$C = \sum f_j C_j \tag{34}$$

When considering thermal conductivity, the combination of materials must account for the orientation of the layers with respect to the direction of heat transport. By extensivity of the heat flux, the average parallel thermal conductivity (i.e. along the y axis on figure 21) is obtained by simple averaging of the contribution of each layers:

$$K_{\parallel} = \sum f_j K_j \tag{35}$$

where K_j is the thermal conductivity of material j. When considering perpendicular thermal conductivity (i.e. along the z axis on figure 21), the resistance to heat transport of each layer, proportional to $1/K_j$, must be used in the average process to ensure conservation of heat flux across the layers. It yields:

$$\frac{1}{K_{\perp}} = \sum \frac{f_j}{K_j} \tag{36}$$

Note that in $K_{\perp}$, the *interfacial thermal resistance* related to the interface between different materials on an atomic scale and the *contact thermal resistance* related to the mechanical homogeneity of the contact between the coil turns have not been accounted for. $K_{\perp}$ is therefore overestimated.

10.3. Joule heating of lamellar structures

Writing I_1/N_c the current circulating in each layer of conductor and using the expression of the total resistance of the coil $R_c = (\rho_{el} L N_c)/(d_c l)$, the total dissipated Joule power is given by:

$$P = \frac{\rho_{el} L N_c}{d_c l} \left(\frac{I_1}{N_c} \right)^2 \tag{37}$$

where ρ_{el} is the electrical resistivity of the conductor. If a constant current is applied during a time t_{on}, the resulting temperature variation of the coil is given by:

$$\Delta T = \frac{P t_{\text{on}}}{L l D C} = \frac{\rho_{el} I_1^2 t_{\text{on}}}{D_c l^2 D C} \tag{38}$$

10.4. Cooling time constants and asymptotic temperature

Based on the lamellar model used here and the distinction between parallel and perpendicular heat transport, the 1D form of the heat equation can be used:

$$\frac{\mathrm{d}T}{\mathrm{d}t} - \frac{K}{C}\frac{\mathrm{d}^2 T}{\mathrm{d}x^2} = 0 \tag{39}$$

If both edges of the considered dimension are in contact with a heat sink at constant temperature T_b, the solution of the heat equation is given by:

$$\begin{cases} T(x,t) & = \sum_{n=1}^{\infty} D_n \sin\left(\frac{n\pi x}{L}\right) \mathrm{e}^{-t/\tau_n} + T_b \\ D_n & = \frac{2}{L}\int_0^L (T(x,0) - T_b) \sin\left(\frac{n\pi x}{L}\right) \mathrm{d}x \\ \tau_n & = \frac{L^2}{n^2\pi^2}\frac{C}{K} \end{cases} \tag{40}$$

Note that D_n is a Fourier component of $T(x,0) - T_b$ on the basis of sine functions compatible with the boundary conditions. The longest-lived mode is the $n = 1$ mode. It defines the cooling time constant $\frac{L^2 C}{\pi^2 K}$. In the particular case of the lamellar model, it yields:

$$\tau_{\parallel} = \frac{L^2 C}{\pi^2 K_{\parallel}} \tag{41}$$

and

$$\tau_{\perp} = \frac{D^2 C}{\pi^2 K_{\perp}} \tag{42}$$

In general, $K_{\perp} \ll K_{\parallel}$ because of the insulator layers, but $L \gg D$ by construction. Since the square of the length is used in the cooling time calculation, the final ordering is $\tau_{\parallel} \gg \tau_{\perp}$.

For an infinity of duty cycles $t_{\text{on}} + t_{\text{off}}$ with $\tau_{\parallel} \gg \tau_{perp} \sim t_{\text{off}} \gg t_{\text{on}}$ and a temperature increase ΔT after each t_{on}, the coil temperature increases up to an asymptotic temperature T_{as}. T_{as} is found by using the conditions $T(x,0) = T_{as} + \Delta T$ and $T(x, t_{\text{off}}) = T_{as}$ in (40):

$$T_{as}(x) = T_b + \sum_{n=1}^{\infty}\left[\sin\left(\frac{n\pi x}{L}\right)\mathrm{e}^{-t_{\text{off}}/\tau_n}\frac{2}{L}\int_0^L (T_{as} + \Delta T - T_b)\sin\left(\frac{n\pi x}{L}\right)\mathrm{d}x\right] \tag{43}$$

Using the ansatz

$$T_{as}(x) = \sum_{n=1}^{\infty} B_n \sin\left(\frac{n\pi x}{L}\right) + T_b, \tag{44}$$

the orthogonality of the basis of sine functions and the space invariance of ΔT, equation (43) results in:

$$B_n = \frac{2\Delta T}{n\pi} \frac{(1-(-1)^n)\mathrm{e}^{-t_{\mathrm{off}}/\tau_n}}{1-\mathrm{e}^{-t_{\mathrm{off}}/\tau_n}} \tag{45}$$

Again, the $n = 1$ component dominates the space dependence of T_{as}. One can therefore write:

$$T_{as}(x) \simeq \frac{4\Delta T}{\pi} \frac{\mathrm{e}^{-t_{\mathrm{off}}/\tau_{\mathrm{cooling}}}}{1-\mathrm{e}^{-t_{\mathrm{off}}/\tau_{\mathrm{cooling}}}} \sin\left(\frac{\pi x}{L}\right) + T_b \tag{46}$$

where τ_{cooling} is the coil cooling time constant. The correct choice for τ_{cooling} depends on the coil design. The heat dissipation at the coil mounting points and the heat transport through the power lines, for example, may have a significant impact on the cooling time. Ignoring the heat transport through mounting points, assuming that the power lines are ideal heat sinks and recalling that $\tau_\perp \ll \tau_\parallel$, the choice $\tau_{\mathrm{cooling}} = \tau_\parallel$ is a good upper limit candidate, even though $\tau_\parallel$ gathers all the coil turns while only one turn is in fact connected to the power lines. If $\tau_\parallel \gg t_{\mathrm{off}}$, equation (46) gives:

$$T_{as}(L/2) \simeq \frac{4}{\pi}\Delta T \frac{\tau_\parallel}{t_{\mathrm{off}}} + T_b \tag{47}$$

10.5. Numerical applications

The choice of material for the coils is GlidCop as conductor and Kapton as insulator. The physical constants of these materials are given in table 3. As a reference, the values for copper are also given.

As in section 9, the 10-turn design and its equivalent 1-turn design are used for the numerical applications. Due to the simple lamellar model used here, the 10-turn design cross-section must nonetheless be adapted to the lamellar design. The coil duty cycle is defined by $t_{\mathrm{on}} = 2\,\mathrm{s}$, $t_{\mathrm{off}} = 20\,\mathrm{min}$ and $I_1 = 7\,\mathrm{kA}$. In addition, the numerical application for a G-coil equivalent is also given. For the G-coil equivalent, since turns are non conjoint, a single turn of length equal to the total winding length and fed with $I_1 = 2\,\mathrm{kA}$ is used to correspond to the coil specifications. In addition, G-coil results are

Parameter	GlidCop	Kapton HN	*Copper*
ρ_m [kg/m^3]	9000	1420	8920
c [J/kg/K]	400	1090	390
C [J/m^3/K]	$3.6 \cdot 10^6$	$1.5 \cdot 10^6$	$3.5 \cdot 10^6$
K [W/m/K]	342	0.12	390
ρ_{el} [Ωm]	$3 \cdot 10^{-8}$	-	$1.7 \cdot 10^{-8}$

Table 3: Physical constants of the materials used to build the coils: GlidCop as conductor and Kapton as insulator. Copper is also given as a reference.

obtained with copper instead of GlidCop. In each case, the first and last layer of the lamellar structure is an insulation layer, so that the insulated mounting points are correctly modelled. The parameters for the different cases are given in table 4. The calculation results are given in table 5.

Parameters	1-turn	10-turns	G-coil equivalent
L [m]	2.42	2.33	20.7
l [m]	0.01	0.01	$8.86 \cdot 10^{-3}$
d_c [m]	0.03	0.003	$8.86 \cdot 10^{-3}$
N_c [m]	1	10	1
D_c [m]	0.03	0.03	$8.86 \cdot 10^{-3}$
d_i [m]	0.0005	0.0005	0.0005
N_i [m]	2	11	2
D [m]	0.031	0.0355	$9.86 \cdot 10^{-3}$
I_1 [kA]	7	7	2

Table 4: Parameters of the different coil designs used in the coil cooling study. L is the coil length, l its width, d_c and d_i are the thicknesses of a layer of conductor and insulator respectively, N_c and N_i are the numbers of layers of each material, D_c is the total conductor thickness, D is the coil thickness and I_1 is the sum of the currents in each turn. For the 10-turn design, L is obtained by averaging the length of the individual coil turns.

10.6. Discussion

- Parallel conduction is not sufficient to ensure cooling of the coils between two heating cycles but the asymptotic temperature might be tolerable depending on the exact coil design.

Parameters	1-turn	10-turns	G-coil equivalent
f_c	97%	85%	90%
f_i	3%	15%	10%
$K_\parallel$ [W/m/K]	331	289	350
$K_\perp$ [W/m/K]	3.68	0.77	1.18
C [J/m^3/K]	$3.53 \cdot 10^6$	$3.28 \cdot 10^6$	$3.28 \cdot 10^6$
$\tau_\parallel$ [s]	6342	6252	407109
$\tau_\perp$ [s]	93.6	542.7	27.4
ΔT [K]	8.9	8.4	6.0
$T_{as} - T_b$ [K]	60	56	2611

Table 5: Results of the thermal characterization of the different coil designs used in the coil cooling study. f_c is the fraction of conductor in the coil, f_i the fraction of insulator, $K_\parallel$ and $K_\perp$ are the parallel and perpendicular thermal conductivity, C the volumetric heat capacity, $\tau_\parallel$ and $\tau_\perp$ are the parallel and perpendicular cooling time constants, ΔT is the temperature variation after t_{on} and $T_{as} - T_b$ is the temperature variation of the center of the coil after an infinite number of heating cycles.

- The perpendicular cooling time is much shorter than the parallel one, so that temperature uniformity across the coil is guaranteed. Note that the lamellar design studied here is the worst case situation for perpendicular heat transport since the number of insulator layers that must be crossed is maximal.

- For coils with multiple turns in contact with one another, the effective length is reduced and the parallel cooling is faster, but not sufficient.

- The worst case is the G-coil. This coil has been successfully used in TCV without cooling for years, but only with short pulses of current in the active part of the cycle.

- Adiabatic temperature increase reaches 9 K per cycle for GlidCop coils and is almost independent of the coil design if the total conductor cross-section is kept constant. Using copper would be beneficial with that respect.

- If the coils can be operated between 100°C and 150°C, the obtained asymptotic temperatures show that no active cooling is necessary for

the saddle coils. However, the calculation assumes a constant temperature at the coil ends, which may result in an underestimation of the asymptotic temperature, and assumes no perpendicular conduction, which may result in an overestimation of the asymptotic temperature. If the assumption of negligible heat conduction is made, 10 to 12 consecutive cycles at maximal current will be tolerated. It might therefore be concluded that no active cooling is necessary but that thermocouples should be included in the coil design to monitor the coil temperature.

- If the design of the coil mounting points results in good thermal contacts between the coil and the vacuum vessel, the length between two mounting points could be used in the calculation of $\tau_{\parallel}$ instead of the whole coil length, as long as $\tau_{\parallel}$ remains much larger than $\tau_{\perp}$.
- Proposed materials are adequate for baking temperature (250°C to 300°C).
- The overall evacuation of heat from the vacuum vessel or portholes should be taken into account in the system design.

11. Conclusion

In this document, two saddle coil system designs have been proposed, namely the in-vessel and the ex-vessel SCS. A number of physical arguments have been suggested to justify the proposed designs in the perspective of applications including RMP, EFC and vertical control and the current requirements have been established for the different applications. A spectral characterization of the proposed SCS has also been done. A wide range of engineering issues have been addressed for the in-vessel design, including the electrical and thermal characterization of the coil system, the magnetic force calculation and an assessment of the consequences of plasma disruptions. While the electromagnetic characterization of the in-vessel design should be of sufficient accuracy, the magnetic forces might have been slightly overestimated in the worst-case approach used in this study. The thermal characterization of the coils has shown that active cooling is not required and that simple monitoring of the coil temperature should be sufficient, thereby loosening coil engineering complexity. The RMP, EFC and vertical control calculations are based on a vacuum field calculation, i.e. excluding plasma response from the model. While this assumption is reasonable and probably

necessary from an engineering point of view, there is no guarantee that it is sufficient to obtain the desired effects on the plasma. The only justification of this assumption is that the SCS design provides features that are similar to other systems (G-coil for vertical control, DIII-D or JET for RMP) when applying the same assumption to these systems. When addressing the question of the choice between an in-vessel and an ex-vessel design, one should keep in mind that although a number of technical challenges have been identified with the in-vessel design, it offers a wider range of experimental applications than the ex-vessel design. In addition, the ex-vessel design also encounters important problems related to space occupation, complex coil geometry and availability of mounting points.

Acknowledgements

This work was supported in part by the Swiss National Science Foundation.

Appendix A. Mutual and self inductance calculation

Appendix A.1. Mutual inductance calculation in general geometry

In general, the mutual inductance between circuits C_i and C_j at a distance r_{ij} from one another is given by Neumann's formula:

$$M_{ij} = \frac{\mu_0}{4\pi} \oint_{C_i} \oint_{C_j} \frac{\mathbf{ds_i} \cdot \mathbf{ds_j}}{|\mathbf{r_{ij}}|} \tag{A.1}$$

where $\mathbf{ds_i}$ and $\mathbf{ds_j}$ are line elements along C_i and C_j. The integral appearing in (A.1) allows a splitting of the circuits in sensible pieces and a reduction of the mutual inductance calculation to these pieces, for example using *ad hoc* analytical formulae. Such an approach greatly reduces the numerical cost of inductance calculation and is used in the case of the SCS.

Note that Neumann's formula assumes thin conductors. In general, reducing the conductors to the path followed by their centers is a good assumption if the minimal distance between both conductors is larger than the cross-section dimensions of the conductors. Calculation shows that this condition can be alleviated and Neumann's formula remains valid when conductors are in contact if the cross-section of the conductors has an aspect ratio equal to 1 (i.e. square or circular). Practically, this means that rectangular cross-section conductors must be split in a subset of square cross-section conductors before performing inductance calculation.

Appendix A.2. Mutual and self inductance of saddle coils

The mutual inductance between two turns of a saddle coil or between two turns of two different coils is calculated by dividing the turns into horizontal arcs of circles and vertical segments. The mutual inductances are calculated between each pair of segments/arcs and the results are combined to obtain the mutual inductances between the turns. Note that the inductance between a vertical segment and a horizontal arc is zero because they are orthogonal to one another. Mathematically, the mutual inductance M is written:

$$M = M_{t_1t_2} + M_{l_1l_2} + M_{b_1b_2} + M_{r_1r_2} - M_{t_1b_2} - M_{b_1t_2} - M_{l_1r_2} - M_{r_1l_2} \quad \text{(A.2)}$$

where turn segments are labelled with t: top, b: bottom, l: left (higher toroidal angle ϕ), r: right (lower toroidal angle ϕ) and $1, 2$ label the turns. The methods used to calculate each terms in equation (A.2) are given in the following sections.

Note that the ex-vessel coils have a particular geometry which involves a number of additional terms in equation (A.2) to account for the horizontal radial segments. These terms are calculated by numerical integration of Neumann's formula and are therefore not described below.

Appendix A.2.1. Mutual inductance between parallel segments

A general analytical formula is given in Grover [37, p. 45] to calculate the mutual inductance between parallel segments. Two segments a and b of lengths l_a and l_b, separated by a perpendicular distance d and having an algebraic length h from the top of a to the bottom of b (h can be negative) have a mutual inductance given without approximation by:

$$\begin{aligned} M = 10^{-7}(&\alpha \mathrm{asinh}\frac{\alpha}{d} - \beta \mathrm{asinh}\frac{\beta}{d} - \gamma \mathrm{asinh}\frac{\gamma}{d} + h \mathrm{asinh}\frac{h}{d} \\ &-\sqrt{\alpha^2+d^2} + \sqrt{\beta^2+d^2} + \sqrt{\gamma^2+d^2} - \sqrt{h^2+d^2}) \end{aligned} \quad \text{(A.3)}$$

with

$$\begin{aligned} \alpha &= l_a + l_b + h \\ \beta &= l_a + h \\ \gamma &= l_b + h \end{aligned} \quad \text{(A.4)}$$

If the segments are aligned ($d = 0$) but have no contact point, another formula is available:

$$M = 10^{-7}(\alpha \ln \alpha - \beta \ln \beta - \gamma \ln \gamma + h \ln h) \quad \text{(A.5)}$$

Finally, if the segments are aligned and juxtaposed ($h = 0$ or $h = -l_a - l_b$), the mutual inductance is given by:

$$M = 10^{-7}(l_a \ln(\frac{l_a + l_b}{l_a}) + l_b \ln(\frac{l_a + l_b}{l_b})) \tag{A.6}$$

If the segments are overlapping, the mutual inductance can be found by calculating the self-inductance of the overlapping bit and combining it with the mutual inductances of the different bits afterwards.

Appendix A.2.2. Self inductance of a straight segment

The self inductance of a conductor can be understood as the average of the mutual inductances of all the filaments it is made of. The value of the inductance is dominated by a term going as $\ln(1/d)$ where d is defined above. The average of the mutual inductances can thus be replaced by the mutual inductance of two segments separated by a distance given by the average of the logarithm of the distances between the filaments, also called the *geometrical mean distance*. Therefore, the self inductance of a segment can be determined through equation (A.3) with $d_{gmd} = 0.2235(w+t)$, $l_a = l_b$ and $h = -l_a$ where w is the width and t the thickness of the segment.

Appendix A.2.3. Mutual inductance between concentric arcs of circles

In the case of arcs of circles, the presence of elliptic integrals in the mutual inductance calculation prevents the formulation of analytical solutions. The best approach consists in using the concentricity of the arcs and the well studied elliptic integrals to simplify the calculation of the mutual inductance. Leduc [38] gives:

$$M_{12} = \frac{\mu_0}{4\pi}\sqrt{r_1 r_2}\int_{\varphi_1}^{\varphi_2} g(k, \frac{\theta}{2} - \frac{\phi_1 + \pi}{2}) - g(k, \frac{\theta}{2} - \frac{\phi_2 + \pi}{2}) d\theta \tag{A.7}$$

with

$$\begin{array}{lcl} k & = & \sqrt{\frac{4r_1 r_2}{(z_1 - z_2)^2 + (r_1 + r_2)^2}} \\ g(k,\theta) & = & (\frac{2}{k} - k)F(k,\theta) - \frac{2}{k}E(k,\theta) \\ F(k,\theta) & = & \int_0^\theta \frac{1}{\sqrt{1 - k^2 sin^2\alpha}} d\alpha \\ E(k,\theta) & = & \int_0^\theta \sqrt{1 - k^2 sin^2\alpha} d\alpha \end{array} \tag{A.8}$$

where $(r_1, z_1, \varphi_1, \varphi_2)$ define the position of the first arc of circle in cylindrical coordinates and $(r_2, z_2, \phi_1, \phi_2)$ the position of the second arc. The elliptic

integrals E and F can be calculated with an AGM method and a Landau transform. The integral on θ is then performed with a standard Simpson method. The implementation of this formulation can be checked with full circle cases and nearly straight segment cases (large radius and small angle).

As in the straight segment case, if the arcs are overlapping, the mutual inductance can be found by calculating the self-inductance of the overlapping bit and combining it with the mutual inductances of the different bits afterwards. However, the 2π-periodicity involved in the calculation leads to a higher level of complexity.

Appendix A.2.4. Self inductance of an arc of circle

As in the straight segment case, the self inductance is calculated with the mutual inductance formulation and the geometrical mean distance.

Appendix A.3. Inductance of turns connected in series

Once the self and mutual inductances of individual turns are known, the effective inductances of individual coils or serial combination of coils can be calculated. If the individual inductances are gathered in matrix $\mathbf{M}$ with M_{ij} the mutual inductance between turns i and j, the effective inductance of the combined system is given by:

$$M_{eff} = \mathbf{T}\mathbf{M}\mathbf{T}^{\mathbf{T}} \tag{A.9}$$

with $\mathbf{T}$ a line vector defined by $T_i = \pm 1$, depending on the sign of the current in the turns.

Appendix B. Resolution of the disruption-induced voltage equation

In order to solve equation (19), the equation system must be diagonalized to decouple the differential equations. One starts by rewriting the first terms of equation (19):

$$\mathbf{R_{ss}}\mathbf{I_s} + \mathbf{M_{ss}}\partial_t\mathbf{I_s} = \mathbf{R_{ss}}^{1/2}\mathbf{R_{ss}}^{1/2}\mathbf{I_s} + \mathbf{R_{ss}}^{1/2}\underbrace{\mathbf{R_{ss}}^{-1/2}\mathbf{M_{ss}}\mathbf{R_{ss}}^{-1/2}}_{\mathbf{K_{ss}}}\mathbf{R_{ss}}^{1/2}\partial_t\mathbf{I_s} \tag{B.1}$$

with $\mathbf{R_{ss}}^{1/2}$ defined as the element-wise square root of the resistance matrix. Since $\mathbf{M_{ss}}$ is symmetric and $\mathbf{R_{ss}}$ is diagonal, $\mathbf{K_{ss}}$ is symmetric. It can

therefore by diagonalized by an orthogonal matrix $\mathbf{T}$: $\mathbf{D_{ss}} = \mathbf{T_{ss}^T K_{ss} T_{ss}}$ and $\mathbf{K_{ss}} = \mathbf{T_{ss} D_{ss} T_{ss}^T}$. The columns of $\mathbf{T_{ss}}$ corresponds to the eigenvectors of $\mathbf{K_{ss}}$ and are found by standard algebraic methods. Using the property that $\mathbf{T_{ss}^T} = \mathbf{T_{ss}^{-1}}$, equation (B.1) is expressed as:

$$\mathbf{R_{ss} I_s} + \mathbf{M_{ss}} \partial_t \mathbf{I_s} = \underbrace{\mathbf{R_{ss}}^{1/2} \mathbf{T_{ss}}}_{\mathbf{A_{ss}}} \underbrace{\mathbf{T_{ss}^T R_{ss}^{1/2}}}_{\mathbf{A_{ss}^T}} \mathbf{I_s} + \mathbf{R_{ss}}^{1/2} \mathbf{T_{ss} D_{ss} T_{ss}^T R_{ss}}^{1/2} \partial_t \mathbf{I_s} \quad \text{(B.2)}$$

giving

$$\mathbf{R_{ss} I_s} + \mathbf{M_{ss}} \partial_t \mathbf{I_s} = \mathbf{A_{ss} A_{ss}^T I_s} + \mathbf{A_{ss} D_{ss} A_{ss}^T} \partial_t \mathbf{I_s} \quad \text{(B.3)}$$

Multiplying (19) to the left by $\mathbf{A_{ss}^{-1}} = \mathbf{T_{ss}^T R_{ss}}^{-1/2}$ therefore gives:

$$\mathbf{I_D} + \mathbf{D} \partial_t \mathbf{I_D} + \mathbf{M_{Dx}} \partial_t \mathbf{I_x} = \mathbf{0} \quad \text{(B.4)}$$

with

$$\mathbf{I_D} = \mathbf{A_{ss}^T I_s} \qquad \mathbf{D} = \mathbf{D_{ss}} \qquad \mathbf{M_{Dx}} = \mathbf{A_{ss}^{-1} M_{sx}} \quad \text{(B.5)}$$

In equation (B.4), the unknowns are decoupled and each differential equation can be solved separately. The solution of equation (B.4) with the assumed plasma current time traces is given by:

$$\mathbf{I_D}(t) = -\frac{1}{\tau} \mathbf{M_{Dx}} \Delta \mathbf{I_x} \cdot \begin{cases} 1 - e^{-t/\mathbf{D}} & t \leq \tau \\ (e^{\tau/\mathbf{D}} - 1) e^{-t/\mathbf{D}} & t > \tau \end{cases} \quad \text{(B.6)}$$

Numerically, the product of exponential terms appearing for $t > \tau$ might be problematic. This difficulty can be avoided by solving for the logarithm of equation (B.6). Once $\mathbf{I_D}(t)$ is known, $\mathbf{I_s}(t)$ is found with:

$$\mathbf{I_s} = \mathbf{R_{ss}}^{-1/2} \mathbf{T_{ss} I_D} \quad \text{(B.7)}$$

References

[1] S. Coda, Progress and Scientific Results in the TCV Tokamak, in: 23rd IAEA Fusion Energy Conference, Daejon, Korea, volume OV, IAEA, pp. 5–2.

[2] G. T. A. Huysmans, ELMs: MHD instabilities at the transport barrier, Plasma Physics and Controlled Fusion 47 (2005) B165–B178.

[3] Y. R. Martin, M. A. Henderson, S. Alberti, P. Amorim, Y. Andrebe, K. Appert, G. Arnoux, R. Behn, P. Blanchard, P. Bosshard, A. Bottino, Y. Camenen, R. Chavan, S. Coda, I. Condrea, A. W. Degeling, V. N. Dokouka, B. P. Duval, D. Fasel, A. Fasoli, J. Favez, S. Ferrando, T. P. Goodman, J.-P. Hogge, J. Horacek, P. Isoz, B. Joye, A. Karpushov, R. R. Khayrutdinov, I. Klimanov, J. B. Lister, X. Llobet, V. E. Lukash, T. Madeira, B. Marletaz, P. Marmillod, A. A. Martynov, S. Y. Medvedev, J.-M. Moret, E. Nelson-Melby, P. Nikkola, P. J. Paris, A. Perez, R. A. Pitts, A. Pochelon, L. Porte, O. Sauter, A. Scarabosio, E. Scavino, S. Seo, U. Siravo, G. Tonetti, M. Q. Tran, L. Villard, H. Weisen, M. Wischmeier, A. Zabolotsky, G. Zhuang, Accessibility and properties of ELMy H-mode and ITB plasmas in TCV, Plasma Physics and Controlled Fusion 45 (2003) A351–A365.

[4] G. Federici, A. Loarte, G. Strohmayer, Assessment of erosion of the ITER divertor targets during type I ELMs, Plasma Physics and Controlled Fusion 45 (2003) 1523–1547.

[5] R. Hawryluk, D. Campbell, G. Janeschitz, P. Thomas, R. Albanese, R. Ambrosino, C. Bachmann, L. Baylor, M. Becoulet, I. Benfatto, J. Bialek, A. Boozer, A. Brooks, R. Budny, T. Casper, M. Cavinato, J.-J. Cordier, V. Chuyanov, E. Doyle, T. Evans, G. Federici, M. Fenstermacher, H. Fujieda, K. G'Al, A. Garofalo, L. Garzotti, D. Gates, Y. Gribov, P. Heitzenroeder, T. Hender, N. Holtkamp, D. Humphreys, I. Hutchinson, K. Ioki, J. Johner, G. Johnson, Y. Kamada, A. Kavin, C. Kessel, R. Khayrutdinov, G. Kramer, A. Kukushkin, K. Lackner, I. Landman, P. Lang, Y. Liang, J. Linke, B. Lipschultz, A. Loarte, G. Loesser, C. Lowry, T. Luce, V. Lukash, S. Maruyama, M. Mattei, J. Menard, M. Merola, A. Mineev, N. Mitchell, E. Nardon, R. Nazikian, B. Nelson, C. Neumeyer, J.-K. Park, R. Pearce, R. Pitts, A. Polevoi, A. Portone, M. Okabayashi, P. Rebut, V. Riccardo, J. Roth, S. Sabbagh, G. Saibene, G. Sannazzaro, M. Schaffer, M. Shimada, A. Sen, A. Sips, C. Skinner, P. Snyder, R. Stambaugh, E. Strait, M. Sugihara, E. Tsitrone, J. Urano, M. Valovic, M. Wade, J. Wesley, R. White, D. Whyte, S. Wu, M. Wykes, L. Zakharov, Principal physics developments evaluated in the ITER design review, Nuclear Fusion 49 (2009) 065012 (15pp).

[6] K. H. Burrell, T. E. Evans, ELM suppression in low edge collisionality

H-mode discharges using n = 3 magnetic perturbations, Plasma Physics and Controlled Fusion 47 (2005) B37–B52.

[7] T. E. Evans, R. A. Moyer, Suppression of large edge localized modes with edge resonant magnetic fields in high confinement DIII-D plasmas, Nuclear Fusion 45 (2005) 595–607.

[8] Y. Liang, H. R. Koslowski, P. R. Thomas, E. Nardon, B. Alper, P. Andrew, Y. Andrew, G. Arnoux, Y. Baranov, M. Bécoulet, M. Beurskens, T. Biewer, M. Bigi, K. Crombe, E. De La Luna, P. De Vries, W. Fundamenski, S. Gerasimov, C. Giroud, M. P. Gryaznevich, N. Hawkes, S. Hotchin, D. Howell, S. Jachmich, V. Kiptily, L. Moreira, V. Parail, S. D. Pinches, E. Rachlew, O. Zimmermann, Active control of type-I edge-localized modes with $n = 1$ perturbation fields in the JET Tokamak, Physical Review Letters 98 (2007) 265004.

[9] E. Nardon, A. Kirk, N. B. Ayed, M. Bécoulet, P. Cahyna, T. Evans, G. Huysmans, H. Koslowski, Y. Liang, S. Saarelma, P. Thomas, ELM control by resonant magnetic perturbations on JET and MAST, Journal of Nuclear Materials 390-391 (2009) 773 – 776. Proceedings of the 18th International Conference on Plasma-Surface Interactions in Controlled Fusion Device.

[10] H. Meyer, R. J. Akers, F. Alladio, L. C. Appel, K. B. Axon, N. B. Ayed, P. Boerner, R. J. Buttery, P. G. Carolan, D. Ciric, C. D. Challis, I. T. Chapman, G. Coyler, J. W. Connor, N. J. Conway, S. Cowley, M. Cox, G. F. Counsell, G. Cunningham, A. Darke, M. Debock, G. Detemmerman, R. O. Dendy, J. Dowling, A. Y. Dnestrovskij, Y. N. Dnestrovskij, B. Dudson, D. Dunai, M. Dunstan, A. R. Field, A. Foster, L. Garzotti, K. Gibson, M. P. Gryaznevich, W. Guttenfelder, N. C. Hawkes, J. Harrison, P. Helander, T. C. Hender, B. Hnat, M. J. Hole, D. F. Howell, M. D. Hua, A. Hubbard, M. Istenic, N. Joiner, D. Keeling, A. Kirk, H. R. Koslowski, Y. Liang, M. Lilley, S. Lisgo, B. Lloyd, G. P. Maddison, R. Maingi, A. Mancuso, S. J. Manhood, R. Martin, G. J. McArdle, J. McCone, C. Michael, P. Micozzi, T. Morgan, A. W. Morris, D. G. Muir, E. Nardon, G. Naylor, M. R. O'Brien, T. O'Gorman, A. Patel, S. D. Pinches, J. Preinhaelter, M. N. Price, E. Rachlew, D. Reiter, C. M. Roach, V. Rozhansky, S. Saarelma, A. Saveliev, R. Scannell, S. E. Sharapov, V. Shevchenko, S. Shibaev, H. Smith, G. E. Staebler, D. Stork,

J. Storrs, A. Sykes, S. Tallents, P. Tamain, D. Taylor, D. Temple, N. Thomas-Davies, A. Thornton, A. Thyagaraja, M. R. Turnyanskiy, J. Urban, M. Valovic, R. G. L. Vann, F. Volpe, G. Voss, M. J. Walsh, S. E. V. Warder, R. Watkins, H. R. Wilson, M. Windridge, M. Wisse, A. Zabolotski, S. Zoletnik, O. Zolotukhin, Overview of physics results from MAST, Nuclear Fusion 49 (2009).

[11] D. A. Gates, Overview of Results from the National Spherical Torus Experiment (NSTX), in: 22nd IAEA Fusion Energy Conference, Geneva, volume OV, IAEA, pp. 3–1.

[12] S. J. Fielding, R. J. Buttery, A. R. Field, P. B. Jones, H. Meyer, M. Valovic, H. R. Wilson, ELM control in COMPASS-D, in: 28th EPS Conference on Controlled Fusion and Plasma Physics, Funchal, volume 25A, pp. 1825 – 1828.

[13] S. M. Wolfe, I. H. Hutchinson, R. S. Granetz, J. Rice, A. Hubbard, A. Lynn, P. Phillips, T. C. Hender, D. F. Howell, R. J. La Haye, J. T. Scoville, Nonaxisymmetric field effects on Alcator C-Mod, Physics of Plasmas 12 (2005) 1–10.

[14] A. Garofalo, K. Burrell, J. Deboo, J. Degrassie, G. Jackson, M. Lanctot, H. Reimerdes, M. Schaffer, W. Solomon, E. Strait, Observation of plasma rotation driven by static nonaxisymmetric magnetic fields in a tokamak, Physical Review Letters 101 (2008).

[15] M. Bécoulet, G. Huysmans, X. Garbet, E. Nardon, D. Howell, A. Garofalo, M. Schaffer, T. Evans, K. Shaing, A. Cole, J.-K. Park, P. Cahyna, Physics of penetration of resonant magnetic perturbations used for Type I edge localized modes suppression in tokamaks, Nuclear Fusion 49 (2009).

[16] K. Shaing, S. Sabbagh, M. Chu, M. Becoulet, P. Cahyna, Effects of orbit squeezing on neoclassical toroidal plasma viscosity in tokamaks, Physics of Plasmas 15 (2008).

[17] H. Reimerdes, O. Sauter, T. Goodman, A. Pochelon, From current-driven to neoclassically driven tearing modes, Physical Review Letters 88 (2002) 1050051–1050054.

[18] O. Sauter, B. P. Duval, L. Federspiel, F. Felici, T. P. Goodman, A. Karpushov, S. Puddu, J. X. Rossel, Effects of ECH/ECCD on Tearing Modes in TCV and Link to Rotation Profile, in: 23rd IAEA Fusion Energy Conference, Daejon, Korea, volume EXS, IAEA, pp. P2–17.

[19] A. Boozer, Equations for studies of feedback stabilization, Physics of Plasmas 5 (1998) 3350–3357.

[20] J. Bialek, A. Boozer, M. Mauel, G. Navratil, Modeling of active control of external magnetohydrodynamic instabilities, Physics of Plasmas 8 (2001) 2170–2180.

[21] C. Bishop, An intelligent shell for the toroidal pinch, Plasma Physics and Controlled Fusion 31 (1989) 1179–1189.

[22] T. Bolzonella, M. Cavinato, E. Gaio, L. Grando, A. Luchetta, G. Manduchi, G. Marchiori, L. Marrelli, R. Paccagnella, A. Soppelsa, P. Zanca, Feedback control of resistive wall modes by saddle coils in RFX-mod, Fusion Engineering and Design 82 (2007) 1064–1072.

[23] J. D. Hanson, Correcting small magnetic field non-axisymmetries, Nuclear Fusion 34 (1994) 441–448.

[24] J. D. Hanson, Using external coils to correct field errors in tokamaks, Plasma Science, IEEE Transactions on 27 (1999) 1588–1595.

[25] J. Rossel, J.-M. Moret, Y. Martin, A 3D multi-mode geometry-independent RMP optimization method and its application to TCV, Plasma Physics and Controlled Fusion 52 (2010).

[26] M. E. Fenstermacher, T. E. Evans, T. H. Osborne, M. J. Schaffer, M. P. Aldan, J. S. deGrassie, P. Gohil, I. Joseph, R. A. Moyer, P. B. Snyder, R. J. Groebner, M. Jakubowski, A. W. Leonard, O. Schmitz, the DIII-D Team, Effect of island overlap on edge localized mode suppression by resonant magnetic perturbations in DIII-D, Physics of Plasmas 15 (2008) 056122.

[27] M. Schaffer, J. Menard, M. Aldan, J. Bialek, T. Evans, R. Moyer, Study of in-vessel nonaxisymmetric ELM suppression coil concepts for ITER, Nuclear Fusion 48 (2008).

[28] M. Bécoulet, E. Nardon, G. Huysmans, W. Zwingmann, P. Thomas, M. Lipa, R. Moyer, T. Evans, V. Chuyanov, Y. Gribov, A. Polevoi, G. Vayakis, G. Federici, G. Saibene, A. Portone, A. Loarte, C. Doebert, C. Gimblett, J. Hastie, V. Parail, Numerical study of the resonant magnetic perturbations for Type I edge localized modes control in ITER, Nuclear Fusion 48 (2008).

[29] P. Cahyna, R. Panek, V. Fuchs, L. Krlin, M. Becoulet, G. Huysmans, E. Nardon, The optimization of resonant magnetic perturbation spectra for the COMPASS tokamak, Nuclear Fusion 49 (2009) 055024 (7pp).

[30] T. E. Evans, R. K. W. Roeder, J. A. Carter, B. I. Rapoport, M. E. Fenstermacher, C. J. Lasnier, Experimental signatures of homoclinic tangles in poloidally diverted tokamaks, Journal of Physics: Conference Series 7 (2005) 174.

[31] E. Nardon, A. Kirk, R. Akers, M. Bécoulet, P. Cahyna, G. De Temmerman, B. Dudson, B. Hnat, Y. Liu, R. Martin, H. Meyer, P. Tamain, D. Taylor, D. Temple, Edge localized mode control experiments on MAST using resonant magnetic perturbations from in-vessel coils, Plasma Physics and Controlled Fusion 51 (2009).

[32] J.-W. Ahn, J. Canik, V. Soukhanovskii, R. Maingi, D. Battaglia, Modification of divertor heat and particle flux profiles with applied 3D fields in NSTX H-mode plasmas, Nuclear Fusion 50 (2010).

[33] E. Nardon, P. Cahyna, S. Devaux, A. Kirk, A. Alfier, E. D. L. Luna, G. D. Temmerman, P. Denner, T. Eich, T. Gerbaud, D. Harting, S. Jachmich, H. Koslowski, Y. Liang, Y. Sun, Strike-point splitting induced by external magnetic perturbations: observations on JET and MAST and associated modelling, Journal of Nuclear Materials In Press, Accepted Manuscript (2010) –.

[34] F. Piras, J.-M. Moret, J. Rossel, Measurement of the magnetic field errors on TCV, Fusion Engineering and Design 85 (2010) 739–744.

[35] J.-K. Park, M. Schaffer, J. Menard, A. Boozer, Control of asymmetric magnetic perturbations in tokamaks, Physical Review Letters 99 (2007).

[36] J.-K. Park, M. Schaffer, R. La Haye, T. Scoville, J. Menard, Error field correction in DIII-D Ohmic plasmas with either handedness, Nuclear Fusion 51 (2011).

[37] F. W. Grover, Inductance Calculations, DvNC, 1946.

[38] P. Leduc, A. Schellmanns, D. Magnon, F. Guitton, Modeling of integrated inductors with a coplanar ground plane using the PEEC method, Microwave Conference, 2003. 33rd European 1 (2003) 447–450 Vol.1.